

1 Differentiation of Vesta: Implications for a shallow magma ocean

2
3 Wladimir Neumann^{*1}, Doris Breuer¹ and Tilman Spohn^{1,2}

4
5 ¹Institute of Planetary Research, German Aerospace Center (DLR)
6 Rutherfordstraße 2, 12489 Berlin, Germany

7
8 ²Institute of Planetology, Westfälische Wilhelm-University Münster,
9 Wilhelm-Klemm-Str. 10, 48149 Münster, Germany

10
11 E-Mail: [*Wladimir.Neumann@dlr.de](mailto:Wladimir.Neumann@dlr.de), Doris.Breuer@dlr.de, Tilman.Spohn@dlr.de

12 *Corresponding Author: Wladimir Neumann, Tel. +493067055395, Fax. +493067055303

13
14 **Draft manuscript for**

15 *Earth and Planetary Science Letters*

16 **Mai 2013**

17
18 **Pages: Main part: 49**

19 **Supplementary material: 8**

20 **Tables: 2**

21 **Figures: Main part: 7**

22 **Supplementary Material: 6**

25 **Proposed Running Head:** Differentiation of Vesta: Implications for a shallow magma ocean

26 **Editorial Correspondence to:**

27 Wladimir Neumann

28 Institute of Planetary Research

29 German Aerospace Center (DLR)

30 Rutherfordstraße 2

31 12489 Berlin

32 Germany

33 Phone: +493067055395

34 Fax: +493067055303

35 E-Mail address: Wladimir.Neumann@dlr.de

36

37

38

39

40

41

42

43

44

45

46

47

48

49

50

51 **Abstract**

52 The Dawn mission confirms earlier predictions that the asteroid 4 Vesta is differentiated with
53 an iron-rich core, a silicate mantle and a basaltic crust, and supports the conjecture of Vesta
54 being the parent body of the HED meteorites. To better understand its early evolution, we
55 perform numerical calculations of the thermo-chemical evolution adopting new data obtained
56 by the Dawn mission such as mass, bulk density and size of the asteroid.

57 We have expanded the thermo-chemical evolution model of Neumann et al. (2012) that
58 includes accretion, compaction, melting and the associated changes of the material properties
59 and the partitioning of incompatible elements such as the radioactive heat sources, advective
60 heat transport, and differentiation by porous flow, to further consider convection and the
61 associated effective cooling in a potential magma ocean. Depending on the melt fraction, the
62 heat transport by melt segregation is modelled either by assuming melt flow in a porous
63 medium or by simulating vigorous convection and heat flux of a magma ocean with a high
64 effective thermal conductivity.

65 Our results show that partitioning of ^{26}Al and its transport with the silicate melt is crucial for
66 the formation of a global and deep magma ocean. Due to the enrichment of ^{26}Al in the liquid
67 phase and its accumulation in the sub-surface (for formation times $t_0 < 1.5$ Ma), a thin shallow
68 magma ocean with a thickness of 1 to a few tens of km forms above which a basaltic crust
69 forms – its thickness depends on the viscosity of silicate melt. The lifetime of the shallow
70 magma ocean is $O(10^4)$ - $O(10^6)$ years and convection in this layer is accompanied by the
71 extrusion of ^{26}Al at the surface. The interior differentiates from the outside inward with a
72 mantle that is depleted in ^{26}Al and core formation is completed within ~ 0.3 Ma. The lower
73 mantle experiences a maximal melt fraction of 45% suggesting a harzburgitic to dunitic
74 composition. Our results support the formation of eucrites by the extrusion of early partial
75 melt and cumulative eucrites and diogenites may form from the crystallizing shallow magma

76 ocean. Silicate melt is present in the mantle for up to 150 Ma, and convection in a
77 crystallizing core proceeds for approximately 100 Ma, supporting the idea of an early
78 magnetic field to explain the remnant magnetisation observed in some HED meteorites.

79

80

81

82

83

84

85

86

87

88

89

90

91

92

93

94

95

96

97

98

99

100

101 **Key Words:** Asteroids, dynamics; Interiors; Meteorites; Planetary formation; Planetesimals.

102 **1. Introduction**

103 The large asteroid 4 Vesta, located in the inner belt at a mean heliocentric distance of 2.36
104 AU, is the second-most-massive body in the asteroid belt. Ground-based observations indicate
105 a dry, basaltic surface composition suggesting that melt segregation and core-mantle
106 differentiation must have taken place and that the body has been resurfaced by basaltic lava
107 flows (e.g., Zellner et al. 1997). The Dawn mission recently orbiting Vesta confirms this
108 observation and the notion that this asteroid is the parent body of the HED (howardite, eucrite
109 and diogenite) meteorites (De Sanctis et al. 2012, Russell et al. 2013). HED's consist mainly
110 of noncumulative eucrites (pigeonite-plagioclase basalts) and orthopyroxene-rich diogenites.
111 Howardites are impact breccias, composed predominantly of eucrite and diogenite clasts. The
112 igneous lithology is completed with more rare rock types that include cumulative eucrites and
113 olivine-bearing diogenites. This lithology has been used to constrain the interior structure.
114 Vesta is believed to have a layered structure consisting of at least a metallic core, a rocky
115 olivine-rich mantle and a crust consisting mainly of an upper basaltic (eucritic) and a lower
116 orthopyroxene-rich layer (e.g., Delany, 1995; Ruzicka et al., 1997; Righter and Drake, 1997;
117 Mandler and Elkins-Tanton, 2013). The details in the interior structure vary between the
118 models and depend among others on the assumption of the bulk composition of Vesta. A
119 eucritic upper crust and orthopyroxene-rich lower crust have been also identified by Dawn in
120 particular in the Rheasilvia basin (De Sanctis et al. 2012, Prettyman et al. 2012). The huge
121 basin allows the identification of material that was formed down to a depth of 30-45 km and
122 has been excavated or exposed by an impact (Jutzi and Asphaug, 2011; Ivanov and Melosh,
123 2013). Interestingly, olivine-rich and thus mantle material has not been found in a significant
124 amount, i.e. not above the detection limit of <25%, suggesting a crustal thickness of at least
125 30-45 km (McSween et al. 2013). This finding may also explain the lack of olivine-rich
126 samples in the HED collection. It should be noted though that several olivine-rich terrains

127 were actually detected by Dawn in the northern hemisphere (De Sanctis et al. 2013, Ruesch et
128 al. 2013).

129 Two possible differentiation scenarios have been associated with the formation of the basaltic
130 achondrites (i.e., eucrites and diogenites). The first scenario suggests that eucrites and
131 diogenites originated from the partial melting of the silicates (e.g. Stolper, 1975, 1977; Jones
132 et al. 1984; Jones et al., 1996) with the extraction of basaltic (euritic) magma leaving behind a
133 harzburgite, orthopyroxenite or dunite residual depending on the degree of partial melting.

134 The other scenario favored by geochemical arguments suggests achondrites being cumulates
135 formed by magma fractionation. In the latter scenario the diogenites could have crystallized
136 either in a magma ocean (Ikeda and Takeda, 1985; Righter and Drake, 1997; Ruzicka et al.,
137 1997; Takeda, 1997; Warren, 1997; Drake, 2001; Greenwood et al., 2005; Schiller et al., 2011)
138 or in multiple, smaller magma chambers (Shearer et al., 1997; Barrat et al., 2008; Beck and
139 McSween, 2010; Mandler and Elkins-Tanton, 2013). Eucrites are then products from the
140 magmas that had earlier crystallized diogenites.

141 Eucrites exhibit siderophile depletions that indicate the formation of an iron-rich core prior to
142 their crystallization and within ~1 to 4 Ma of the beginning of the solar system (Palme and
143 Rammensee 1981; Righter and Drake 1997, Kleine et al., 2009). Assuming core densities
144 between 7000 and 8000 kg m⁻³, the core radius of Vesta is estimated to lie between 105 and
145 114 km (Raymond et al. 2012, Russell et al. 2012), approximately half of the asteroid's
146 radius. Some HEDs (e.g. Millbillillie and Allan Hills A81001), furthermore, show a remnant
147 magnetisation suggesting a formerly active dynamo in a liquid metallic core (Fu et al.
148 2012a,b).

149 To understand Vesta's thermal and geological evolution, several numerical and experimental
150 studies (e.g. Righter and Drake 1997, Ghosh and McSween 1998, Drake 2001, Gupta and
151 Sahijpal 2010) have been performed. Questions these studies want to answer are related to the
152 timing of accretion and core formation and the history of volcanism, especially the formation

153 of the basaltic crust. Related to the last issue is in particular the question about the origin of
154 the HED meteorites that either originated from the partial melting of the silicates or are
155 residual melts of a crystallizing and formerly convecting whole-mantle magma ocean. It
156 should be noted though that in most models the formation of core and crust has not been
157 modelled self-consistently; rather some specific scenario has been assumed and its
158 consequences for the thermal evolution on Vesta have been studied.

159 Righter and Drake (1997) considered core formation and crystallisation of a cooling magma
160 ocean using a numerical physicochemical model. They suggested that after cooling to a
161 crystal fraction of 80%, residual melt percolated from the former extensive magma ocean to
162 form eucrites at the surface and diogenites in shallow layers by further crystallisation. In their
163 model complete crystallisation occurred within 20 Ma after the formation of Vesta.

164 Ghosh and McSween (1998) investigated the differentiation of Vesta by assuming
165 instantaneous core formation in the temperature interval of 1213-1223 K (assumed solidus
166 and liquidus temperature of Fe-FeS) and that HED meteorites are the product of 25% partial
167 melting. To obtain such a scenario, they concluded that Vesta must have accreted at 2.85 Ma,
168 differentiated at 4.58 Ma and formed a basaltic crust at 6.58 Ma relative to the formation of
169 the CAIs. Furthermore, they suggested that the mantle remained hot for 100 Ma after its
170 formation and that some near-surface layers may have remained undifferentiated.

171 The latter models suggesting a global magma ocean have in common that they neglect
172 efficient cooling due to convection in the magma ocean and partitioning of ^{26}Al into the
173 silicate melt and of its migration towards the surface. So far, there have not been many
174 attempts to model magma ocean convection in planetesimals,. A first model to study the
175 influence of a convecting magma ocean that formed due to heating by ^{26}Al in planetesimals
176 with radii of less than 100 km was presented by Hevey and Sanders (2006). Convection and
177 the associated heat transport have been simulated by increasing the thermal conductivity by
178 three orders of magnitude upon reaching a melt fraction of 50% - at this rheologically critical

179 melt fraction (RCMF) a strong decrease in the viscosity is expected resulting in vigorous
180 convection and efficient heat transport (Marsh, 1988). As an important consequence, it has
181 been shown that the excess radiogenic heating does not raise the temperature of the
182 convecting interior and thus the degree of partial melting in the magma ocean but rather
183 increases the extent of the molten zone.

184 Gupta and Sahijpal (2010) adopted this approach in their simulations for Vesta by varying the
185 thermal diffusivity by three orders of magnitude between the melt fractions of 50% and 100%
186 (thereby, the thermal conductivity was increased). They investigated two evolution paths,
187 namely the formation of basaltic achondrites in Vesta via partial melting of silicates or as
188 residual melts after crystallisation of a convecting magma ocean. They concluded that,
189 depending on the formation time, melt extraction is possible between 0.15 and 6 Ma after the
190 CAIs and that differentiation proceeds rapidly within $O(10^4)$ a. For the scenarios where
191 accretion was completed within 2 Ma after the CAIs, a magma ocean formed, which does not
192 crystallise completely for at least 6-10 Ma. We will later show that for magma oceans
193 comprising a large part of the mantle, the convective heat flux is underestimated in the studies
194 Hevey and Sanders (2006) and Gupta and Sahijpal (2010) in comparison to that of the soft
195 turbulence regime that is valid when the viscosity is small and convection is extremely
196 turbulent as in the case of magma oceans (Solomatov, 2007). In fact, as we point out further
197 below, the effective thermal conductivity of the magma ocean is underestimated by up to
198 three orders of magnitude.

199 The importance of equilibrium partitioning of ^{26}Al into the silicate melt and of its migration
200 toward the surface has been shown by Moskovitz and Gaidos (2011) for planetesimals smaller
201 than Vesta. They concluded that migration of ^{26}Al -enriched melt towards the surface inhibits
202 a further increase of internal temperatures and partial melting. In their model, only subsequent
203 heating by ^{60}Fe generates melt fractions of over 50% completing the differentiation of the
204 bodies of interest. Although Vesta was not considered in their study, the partitioning of ^{26}Al ,

205 its extrusion to the surface and the associated depletion of the interior would have a strong
206 impact on its thermal evolution.

207 As a general conclusion from the previous thermal models one can state that Vesta should
208 have finished its accretion by ≈ 3 Ma after the CAIs due to the decrease of the radiogenic
209 heating by ^{26}Al and ^{60}Fe with time. Whether the basaltic crust, i.e. eucrites and diogenites, did
210 form after the core-mantle separation due to the crystallisation of a global magma ocean
211 (residual melt origin) or prior to the core-mantle separation due to the extrusion of the first
212 partial melts (partial melting origin) remains an open issue, although geochemical models
213 suggest that core formation precedes crust formation (e.g. Kleine et al., 2009). Which scenario
214 is more likely also depends on the competition between heating by short-lived isotopes and
215 the depletion of these heat sources due to their partitioning into the melt and the migration
216 velocity of this melt by porous flow. Only if the extrusion of melt containing ^{26}Al is
217 comparatively slow an asteroid-scale magma ocean may have formed, otherwise HEDs
218 formed by the extrusion of early partial melts. In case of a magma ocean, its convective
219 cooling and the associated thermal convection in the core could result in a core dynamo
220 lasting for several 10 Ma if Vesta formed before ≈ 1.5 Ma after the CAIs (Elkins-Tanton et al.
221 2011) although Sterenborg and Crowley (2013) argue that only parent bodies larger than 500
222 km can produce a sufficient strong magnetic field longer than 10 Ma by thermal convection.

223 In the present study, we investigate the thermal evolution of Vesta by means of a
224 comprehensive model that includes melting, associated changes of the material properties,
225 differentiation via porous flow and the corresponding advective heat transport below the
226 RCMF of 50% (Marsh, 1988), as well as convection and the associated effective cooling in a
227 magma ocean and liquid core for melt fractions above the RCMF applying the soft-turbulence
228 approach (Solomatov et al., 2007). Numerical calculations of the thermo-chemical evolution
229 of Vesta are performed adopting the new data obtained by the Dawn mission (e. g. the mass,
230 the bulk density and the dimensions, see Russell et al. 2012). In particular, we investigate the

231 occurrence and the time scale of core-mantle differentiation, the differences between the
232 models that consider partitioning of ^{26}Al and those that neglect partitioning of ^{26}Al , as well as
233 the influence of the convecting magma ocean on the thermal evolution of Vesta. We conclude
234 that due to the extrusion of ^{26}Al towards the surface a thin sub-surface magma ocean forms
235 prior to the completion of the core-mantle differentiation and that the depleted mantle remains
236 below the RCMF.

237 **2. Model description**

238 The evolution of an asteroid begins with its accretion from the protoplanetary dust as a porous
239 aggregate. Heating by radioactive decay combined with self-gravity leads to substantial
240 compaction at sub-solidus temperatures. Provided strong heating, the metal phase and
241 subsequently the silicate phase starts to melt upon reaching the respective solidus
242 temperatures. The radioactive isotope ^{26}Al partitions among other incompatible elements into
243 the silicate melt. If melting is wide-spread enough, the asteroid can differentiate (at least
244 partially) via porous flow into a metallic core and a silicate mantle. Differentiation is initiated
245 by the iron melt sinking downward and silicate melt percolating towards the surface. The
246 mantle and core regions, in which the partial melt increases above 50%, start convecting.
247 Furthermore, convection starts only when the heat flow at the upper interface becomes super-
248 adiabatic – this is in particular a limiting factor for convection in the core. The asteroid cools
249 due to convection and after the melt fractions drop below 50% by conduction and melt heat
250 transport to the sub-solidus temperatures. After cooling below the solidus, no further
251 structural changes (differentiation) of the interior can be expected except by external
252 influence such as impacts.

253 To model the above evolution path for Vesta, we have adopted the thermal evolution model
254 from Neumann et al. (2012) which considers accretion, compaction, melting and
255 differentiation by porous flow of ordinary chondritic planetesimals. For a detailed description

256 of the model we refer to Neumann et al. (2012) and Neumann et al. (2013). Next, we give a
 257 brief summary of the important model features and describe in particular the additional
 258 processes implemented for the current study as well as the parameters that are specific for
 259 Vesta.

260 The rate of change of internal energy, including the consumption and release of latent heat
 261 due to melting and solidification is computed from the conductive heat flow, the volumetric
 262 heat production rate by radioactive decay, and the advective heat transport by melt
 263 percolation:

$$264 \quad \rho c_p (1 + x_{Fe} Ste_{Fe} + x_{Si} Ste_{Si}) \frac{\partial T}{\partial t} = \vec{\nabla} \cdot (k(\vec{x}) \vec{\nabla} T) + Q(\vec{x}, t) + \vec{\nabla} T \cdot (\Delta v_{Fe} + \Delta v_{Si}), \quad (1)$$

265 where ρ is the density, c_p is the specific heat capacity, x_{Fe} and x_{Si} are the current mass fractions
 266 of metallic iron and silicates, respectively, Ste_{Fe} and Ste_{Si} are the Stefan numbers of metal and
 267 silicates, respectively, T is temperature, t is time, \vec{x} is the space variable, k is the thermal
 268 conductivity, Q is the heat source density, and Δv_{Fe} and Δv_{Si} are the velocities of iron and
 269 silicate melts relative to the matrix, respectively.

270 Because we consider porosity loss during the thermal evolution, the initial radius R_p of the

271 body changes to the compacted radius $\bar{R}_p(t) = R_p \left(\frac{1 - \phi_0}{1 - \bar{\phi}(t)} \right)^{1/3}$, where $\bar{\phi}(t)$ is the average

272 porosity at time t , and ϕ_0 is the uniform initial porosity. The average porosity $\bar{\phi}(t)$ and the
 273 average density $\bar{\rho}(t)$ are computed using the equations $\bar{\phi}(t) = 1 - V_i/V_b$ and $\bar{\rho}(t) = M/V_b$ where
 274 V_i is the intrinsic volume (i.e., the volume of the solid material), V_b is the bulk volume (i.e.,
 275 the volume of the solid material plus the volume of the pores, computed by integrating the
 276 porosities at the grid points of the discretisation over the body) and M is the mass of Vesta.

277 The thermal conductivity, density, heat source density, radius, and some other parameters
 278 change with time due to the loss of porosity and melting. The loss of the porosity ϕ is a
 279 consequence of compaction by hot-pressing under the influence of temperature and pressure:

280
$$\frac{\partial \log(1 - \phi(\bar{x}))}{\partial t} = A\sigma^{2/3}b^{-3}e^{-E/RT}, \quad (2)$$

281 where $A=4.0 \cdot 10^{-5}$ is a constant, σ is the effective stress acting on a unit volume, b is the initial
 282 grain size, E is the activation energy, and R is the universal gas constant.

283 Iron or silicate melt is generated linearly between the solidus and the liquidus temperatures of
 284 metal or silicates. In this temperature interval both components are present in both solid and
 285 liquid states. Consumption and release of the latent heat during the melting and solidification
 286 buffers temperature variations between the entirely solid and the entirely liquid state.

287 In terms of the flow in porous media theory, we relocate the intrinsically denser (than the bulk
 288 solid matrix) metal melt downwards, and the intrinsically lighter silicate melt towards the
 289 surface, according to Darcy's law. This approach is valid below the RCMF. In this case, the
 290 energy transport by the melts enters into the heat conservation equation via advection terms.
 291 Thereby, the associated grain growth due to Ostwald ripening is accounted for in the partially
 292 molten regions of the body resulting in faster percolation velocities with time.

293 Assuming equilibrium melting, the chemical partitioning of ^{26}Al is described by

294
$$c_{Al}^{tot} = \chi_{Si}c_{Al}^l + (1 - \chi_{Si})c_{Al}^s, \quad c_{Al}^l = \frac{c_{Al}^{tot}}{P + \chi_{Si}(1 - P)}, \quad c_{Al}^s = \frac{c_{Al}^{tot}P}{P + \chi_{Si}(1 - P)}, \quad (5)$$

295 with the total concentration of ^{26}Al c_{Al}^{tot} , the concentration in the solid and liquid

296 phase c_{Al}^s and c_{Al}^l , the melt fraction of silicates (relative to the overall amount of silicates) χ_{Si} ,

297 and the partitioning coefficient P (Best, 2002).

298 To calculate the initial composition of the primordial material we assume that Vesta formed
 299 from L-chondritic material. The minerals, their mass fractions and densities are taken from

300 Yomogida and Matsui (1983) (see Table 1). The metal phase consists of free iron and nickel

301 and of the troilite. The remaining minerals form the silicate phase. This composition is a

302 reasonable choice considering Dawn's measurements of the density. First, a metal mass

303 fraction of 0.14 in an L-chondritic composition results in a relative core radius of ≈ 0.43 if one

304 assumes complete differentiation, which agrees with the core radius of Vesta suggested by
 305 Russell et al. (2012). Note that for an H-chondritic composition a larger core with a relative
 306 core radius of ≈ 0.49 would follow (cf. Neumann et al. 2012). Second, the average bulk
 307 density of $3456 \pm 34 \text{ kg m}^{-3}$ (Russell et al. 2012) lies slightly below a typical intrinsic density
 308 of an L-chondrite (see Yomogida and Matsui 1983), which is approximately 3600 kg m^{-3} (cp.
 309 Table 1).
 310 Heavy cratering of the surface suggests a porous upper mantle and crust. Russell et al. (2012)
 311 suggested a porosity of 5-6% in these layers, which means that the average porosity of the
 312 entire body is smaller. From $\rho_i = \rho_b (1 - \phi)^{-1}$ where ρ_i is the average intrinsic density and ρ_b is
 313 the bulk density, the average porosity of Vesta ϕ can be calculated. For $\rho_b = 3490 \text{ kg m}^{-3}$
 314 which is the smallest upper bound we obtain $\phi = 0.03$ and for $\rho_b = 3456 \text{ kg m}^{-3}$,
 315 $\phi = 0.04$ follows. This would mean that the average porosity of the mantle and the crust of
 316 Vesta is larger than 4%. The bulk density ρ_{b0} of the primordial material during the accretion
 317 of Vesta is calculated by using a reasonable uniform initial porosity $\phi_0 = 0.4$ of the accreting
 318 material (see Henke et al. 2012, Neumann et al. 2012) and the equation $\rho_{b0} = (1 - \phi_0) \rho_i$. For
 319 $\rho_i = 3600 \text{ kg m}^{-3}$ we obtain $\rho_{b0} = 2160 \text{ kg m}^{-3}$.
 320 Taking the volume of Vesta as $7.497 \times 10^7 \text{ m}^3$ (Russell et al. 2012) and assuming a negligible
 321 average porosity (in our most realistic calculations Vesta compacted almost completely; this
 322 is a result of our model runs) a radius of 262 km is obtained. We take this as a reference value
 323 which corresponds to a completely compacted body. For an appropriate choice of the average
 324 present-day porosity the value of 262.7 ± 0.1 inferred by Russell et al. (2012) follows. Note
 325 though that a body with the axes of 572.6 by 557.2 by 446.4 km is considered here to be
 326 spherically symmetric. Our model combines the average (uniform) initial porosity of
 327 $\phi_0 = 0.4$ with the reference radius of $D = 262 \text{ km}$ to obtain the initial radius of $R_p = 310 \text{ km}$.

328 For melt fractions above 50%, the settling velocity v_s of the molten iron globules or solid iron
329 crystals in a silicate mush is computed via Stokes' law

$$330 \quad v_s = \frac{2}{9} \frac{\rho_g - \rho_m}{\eta_{l,si}} g b^2, \quad (3)$$

331 where ρ_g is the density of a metal globule (liquid iron), ρ_m is the density of the silicate mush
332 (liquid silicate), $\eta_{l,si}$ is the viscosity of the liquid silicates, g is the gravitational acceleration
333 and b is the radius of a metal globule (here a constant value of 0.01 m is adopted, see e.g.
334 Samuel, 2012 and Taylor, 1992 for the globule size). Strictly speaking, further dynamic
335 regimes (Newton and intermediate regimes, see Samuel, 2012) should be considered besides
336 the Stokes regime. Our estimates using parameters from Tables 1 and 2 indicate that the
337 velocities obtained in the Stokes, Newton or intermediate regimes are very similar and much
338 higher compared to the Darcy velocity obtained below the RCMF (the latter is orders of
339 magnitude smaller). The metal separation is thus almost instantaneous for the situation of high
340 melt fraction and we therefore consider only the Stokes regime.

341 Throughout the study the nebula temperature of $T_n=290$ K (this value corresponds to the
342 temperature in the Solar nebula at 2.36 AU, see Ghosh and McSween 1998) is used as the
343 initial temperature of the accreting material and also for the boundary condition. The radiation
344 boundary condition is adopted with the emissivity $e=0.8$ (Ghosh and McSween 1998).

345 For a body which formed during the first few million years after the formation of the Solar
346 system the short-lived isotopes ^{26}Al and ^{60}Fe are believed to be the most important heat
347 sources. Whereas most researchers suggest the "canonical" ratio $[^{26}\text{Al}/^{27}\text{Al}]_0=5 \times 10^{-5}$ at the
348 time of the formation of CAIs, there is still an uncertainty about the initial ratio $[^{60}\text{Fe}/^{56}\text{Fe}]_0$
349 (values between 10^{-8} and 10^{-6} have been inferred by numerous workers). For ^{26}Al we use the
350 canonical ratio $[^{26}\text{Al}/^{27}\text{Al}]_0=5 \times 10^{-5}$ at the formation of the CAIs, and for ^{60}Fe the value
351 $[^{60}\text{Fe}/^{56}\text{Fe}]_0=1.6 \times 10^{-6}$ reported by Cameron (1993). As this value is highly uncertain and
352 recent experiments suggest that previous measurements are likely biased and predict to high

353 values of $[\text{}^{60}\text{Fe}/\text{}^{56}\text{Fe}]_0$ (Ogliore et al., 2011; Telus et al., 2012), we further study the influence
 354 of the amount of ${}^{60}\text{Fe}$ on the results.

355 Apart from the initial ratios above, the heat production rate depends on the abundance of Al
 356 and Fe in the bulk material. The latter are computed from the exact composition and fractions
 357 of metal and silicates (see further below). The heat sources density term $Q(r,t)$ in the energy
 358 balance equation (1) arises from the radiogenic decay of ${}^{26}\text{Al}$ and ${}^{60}\text{Fe}$. We write this term as

$$359 \quad Q(r,t) = \rho \left(v_{Si} \left[\frac{{}^{26}\text{Al}}{{}^{27}\text{Al}} \right] \frac{E_{Al}}{\tau_{Al}} e^{-\frac{t+t_0}{\tau_{Al}}} + \frac{x_{Fe}}{x_{Fe,0}} f_{Fe} \left[\frac{{}^{60}\text{Fe}}{{}^{56}\text{Fe}} \right] \frac{E_{Fe}}{\tau_{Fe}} e^{-\frac{t+t_0}{\tau_{Fe}}} \right), \quad (4)$$

360 where $v_{Si} = f_{Al} x_{Si}/x_{Si,0}$ (prior to silicate melting, partitioning and melt segregation), $x_{Fe,0}$ and
 361 $x_{Si,0}$ are the initial mass fractions of metal and silicates, f_{Fe} and f_{Al} is the number of iron or
 362 aluminium atoms per 1 kilogram of the primordial material, respectively, E_i is the decay
 363 energy per atom, τ_i is the mean life, $[{}^*i/{}^*i]_0$ is the initial abundance of the isotope *i , and t_0 is
 364 the delay time of accretion with respect to the formation time of the CAIs. The mass fraction
 365 ratios control the changes in the heat production due to the differentiation. The bulk Al mass
 366 fraction is calculated from that of Al_2O_3 in L-chondrites reported by Jarosevich (1990). The
 367 latter value of 0.0225 is multiplied with the ratio of the atomic mass of ${}^{27}\text{Al}$ (in g mol^{-1}) times
 368 two, and the sum of the atomic masses of ${}^{27}\text{Al}$ times two and ${}^{16}\text{O}$ times three, to obtain the
 369 value of 0.0119. This is slightly larger than the value of 0.0113 used by Ghosh and McSween
 370 (1998) for Vesta, because they assumed an H-chondritic composition and adopted the Al_2O_3
 371 mass fraction of 0.0214 from Jarosevich (1990).

372 The mass fraction of the bulk iron is computed from the mass fraction of the free iron Fe and
 373 the mass fraction of FeS times the ratio of the atomic mass of Fe and the sum of the atomic
 374 masses of Fe and S. Thereupon, the (initial) abundances are computed using the formulas
 375 $f_{Al} = 10^3 m_{Al} N_A (m a_{26Al})^{-1}$ (before melting and partitioning) and $f_{Fe} = 10^3 m_{Fe} N_A (m a_{60Fe})^{-1}$, where
 376 m_{Al} and m_{Fe} are mass fraction of the elements, $m a_{26Al}$ and $m a_{60Fe}$ are the atomic masses of

377 the heat generating isotopes, and N_A is the Avogadro number (for the resulting values see
 378 Table 2). The factor v_{Si} controls on the one hand the changes in the silicate mass fraction due
 379 to the migration of the silicate melt as compared to the initial mass fraction. On the other
 380 hand, this factor updates the changes in the concentration of ^{26}Al in a given discretisation
 381 shell, which arise from the mixing of migrated and present melt with different concentration
 382 of ^{26}Al and from the matrix compaction. Once melt segregation starts, ^{26}Al particles
 383 associated with the migrated silicate melt from a lower shell are added to those remaining in
 384 the upper shell after the compaction of the mixed metal-silicate-matrix. The number of ^{26}Al
 385 particles in the lower shell is updated to account for the ^{26}Al that left with the silicate melt and
 386 the particles added due to the matrix compaction. Similarly, as iron melt moves from an upper
 387 shell to a lower one and is being replaced by either a certain volume of the matrix or/and a
 388 certain volume of the silicate melt, the number of ^{26}Al particles is updated due to these
 389 volume changes. We have neglected the heating by ^{60}Fe which remains in the silicate phase
 390 after core formation, its contribution to the heating of the mantle is, however, negligible.
 391 As in the previous studies, we do not consider the solid-state convection for melt fractions
 392 below 50%. In order to model the convection in a magma ocean, where more than 50% of the
 393 material is molten, we adopt the method presented in Solomatov (2007) (see also Kraichnan
 394 1962 and Siggia 1994) to compute the convective heat flux in the soft turbulence regime
 395 (when the viscosity is small and convection is extremely turbulent, but the Rayleigh number is
 396 still below approximately 10^{19}). This approach has also been used for modelling of local
 397 magma ponds on Mars (Golabek et al. 2011). From the convective heat flux the effective
 398 thermal conductivity is calculated. The thermal conductivity in the magma ocean is
 399 substituted by the effective thermal conductivity, which mimics the heat flux of a medium
 400 with a low magma ocean viscosity:

$$401 \quad k_{\text{eff}} = F_{\text{conv}} L / \Delta T, \quad (5)$$

402 where F_{conv} is the convective heat flux, L is the depth of the magma ocean and $\Delta T = T_p - T_s$, with
 403 the potential temperature T_p and the temperature T_s at the upper boundary of the magma
 404 ocean. In a silicate magma ocean this temperature corresponds to the silicate melt fraction of
 405 50% and is equal to 1637 K. In a convecting core this is the temperature at the core-mantle
 406 boundary or at the upper boundary of the convecting part of the core. The latter is equal to or
 407 higher than the temperature of 1456 K which corresponds to the iron melt fraction of 50 %.
 408 In the following we use the index i which is either Fe or Si to distinguish between a silicate
 409 magma ocean in the mantle and a convecting (part of the) core. The convective heat flux in
 410 the soft turbulence regime may be expressed as follows:

$$411 \quad F_{\text{conv},i} = 0.089 k_i (T_{p,i} - T_{s,i}) \text{Ra}_i^{1/3} / L_i, \quad (6)$$

412 where k_i is the thermal conductivity and Ra_i is the Rayleigh number. The Rayleigh number is
 413 computed from

$$414 \quad \text{Ra}_i = \frac{\alpha_i g_i (T_{p,i} - T_{s,i}) \rho_i^2 c_{p,i} L_i^3}{k_i \eta_{l,i}} \quad (7)$$

415 where α_i is the thermal expansivity, g_i is the surface gravity of the respective convecting layer,
 416 ρ_i is the density, $c_{p,i}$ is the heat capacity, and $\eta_{l,i}$ is the viscosity of the melt.

417 Convection in the core is treated in a similar manner. Here, if the heat flux at the core-mantle
 418 boundary from the core into the mantle is positive and climbs above the adiabatic heat flux at
 419 the CMB, and the melt fraction in the core is above the RCMF, thermal convection is
 420 assumed to occur (Stevenson 2003). This is achieved by solving equations (5)-(7) using the
 421 parameters of the core.

422 The adiabatic heat flow at the radius $r = r_{\text{CMB}}$ (corresponding to the core-mantle boundary) is
 423 computed from the equation

$$424 \quad k_c (dT/dr)_{\text{ad,CMB}} = k_c \alpha_c T_{\text{CMB}} g_{\text{CMB}} / c_{pc}, \quad (8)$$

425 where the index “c” denotes the core parameters, and the index “CMB” the parameters taken
426 at the core-mantle boundary. Note that if only a part of the core is convecting, the respective
427 parameters are not taken at the CMB, but at the upper boundary of the involved zone. For the
428 parameters see Table 1 and Table 2. We have tested the numerical code against existing codes
429 in the literature. Details about these tests, the time discretization and the chosen resolution can
430 be found in the Supplementary Material.

431 **3. Results**

432 In first sample runs with purely conductive heat transport (thus neglecting differentiation, heat
433 transport by porous flow and convection in a magma ocean) we obtain a crude upper bound of
434 the formation time $t_0=2.9$ Ma relative to the CAIs for the existence of a core - the solidus
435 temperature of the silicate phase is exceeded in the centre of Vesta for formation times of up
436 to 2.4 Ma and that of the metal phase for $t_0\leq 2.9$ Ma relative to the CAIs (see Fig. 1). This
437 upper boundary value can be refined if one considers differentiation.

438 Due to the effective radiogenic heating and the small surface-to-volume ratio the temperature
439 in the mantle can reach several thousand degrees. Mantle temperatures exceeding the liquidus
440 temperature of 1850 K of silicates are obtained for formation times of $t_0\leq 2$ Ma after the CAIs
441 but are inconsistent with the conclusions of Mason (1962), Stolper (1975,1977), Jones et al.
442 (1984) and Jones et al. (1996), who suggest that the eucrites were generated by no more than
443 25% partial melting of the source region (noncumulative eucrite Sioux County, see Jones et
444 al. 1996) and that 25% partial melting of the primordial mantle generated the crust. If one
445 investigates the thermal evolution of Vesta without any additional cooling mechanisms except
446 conduction, the only way to satisfy the physical constraints (e.g. 25% of silicate melting) is by
447 assuming that Vesta formed at least 2 Ma after the CAIs. In this manner the thermal evolution
448 of Vesta was investigated e. g. in Ghosh and McSween (1998). However, higher melt

449 fractions could theoretically have been achieved in the source region after the extraction of
450 melts which formed the eucrites.

451 Considering in a next step differentiation, partitioning of radioactive heat sources, heat
452 transport by porous flow and convection, the thermo-chemical evolution differs significantly.
453 Because ^{26}Al is an incompatible element and is saturated in the liquid silicate phase during the
454 melting of the silicates, the migration of the silicate melt has notable effects on the thermal
455 evolution if this process is considered, because the concentration of ^{26}Al becomes non-
456 constant during and after the differentiation at different radii. Values of down to 0.003 have
457 been suggested for the partitioning coefficient P , which controls the concentrations of ^{26}Al in
458 the solid and in the liquid silicate phase (Kennedy et al. 1993, Pack and Palme 2003). In the
459 present study, we adopt the value $P=0.02$ to avoid a possible bias of the results.

460 The following scenario applies to a formation time $t_0 < 1.0$ Ma after the CAIs (see Fig. 2). In
461 the early stages of the differentiation, when the first silicate melt is produced, ^{26}Al -rich melt
462 migrates towards the surface (at temperatures slightly above the silicate solidus of 1425 K)
463 causing saturation of ^{26}Al in a shallow sub-surface layer, whereas the solid matrix, which is
464 depleted in ^{26}Al , compacts downwards. In a shallow layer temperature increases rapidly due
465 to the strongly enhanced production of radiogenic heat (see Fig. 3 and 4). Directly below a
466 rigid undifferentiated shell the melt fraction rises up to the RCMF and convection starts in an
467 approximately 1 km thick magma ocean. Close vicinity of the surface and effective cooling
468 prevent the magma ocean from including the surface.

469 Directly above this superheated sub-surface layer and below the undifferentiated shell a
470 region forms where silicate melt fractions lie below 50% and porous flow takes place. In this
471 extremely thin boundary layer ^{26}Al saturated melt percolates to the surface. Convection and
472 efficient cooling through the surface causes the potential temperature in the magma ocean to
473 vary around 1637 K (at this temperature 50% of the material in the silicate magma ocean is
474 molten and thus the RCMF is crossed) resulting in a fluctuation between convective and

475 advective regimes. In the advective regime the ^{26}Al particles contained in the magma ocean
476 migrate by porous flow into the boundary layer. This way, even more ^{26}Al rises to the surface
477 from the boundary layer together with the erupting silicate melt. Still, due to the
478 differentiation which takes place further below, additional ^{26}Al is transported into the magma
479 ocean, which is subsequently heated above the critical temperature and switches again from
480 the advective to the convective regime. Not all radioactive material leaves the mantle, nor
481 does all of it reside at the surface. As soon as some portion of melt extrudes, it covers a part of
482 the ^{26}Al -enriched crustal material. We assume that this material transports ^{26}Al into the
483 boundary layer. This way material circulation between the surface and the boundary layer is
484 established such that the critical temperature of 1637 K and thus a sub-surface magma ocean
485 can be maintained right below the thin crust for as long as $O(10^4)$ - $O(10^5)$ a. This mechanism
486 leads to a substantial reduction of heating throughout the body as the major part of the
487 radioactive material (except ^{60}Fe) is involved in the material circulation between the crust and
488 the upper mantle (here the crust is a solid basaltic carapace, the mantle is the layer with less
489 than 1 vol% metal, the core is the central area with less than 1 vol% silicates). The sub-
490 surface is the first completely differentiated part of the planetesimal. Simultaneously the
491 differentiation of the deeper layers proceeds. Thereby the upper mantle is first cleared of the
492 metal, then the rest of the mantle and the metal core form simultaneously.

493 The last stage of the silicate-metal differentiation is the formation of a distinct core-mantle
494 boundary. After less than 0.3 Ma from the start of the melt migration, core formation is
495 completed (e. g. for $t_0=0$ Vesta differentiates between 0.17 Ma and 0.33 Ma, for $t_0=0.5$ Ma
496 between 0.78 Ma and 1 Ma, and for $t_0=1$ Ma between 1.5 Ma and 1.72 Ma). As a consequence
497 of the depletion in ^{26}Al of the mantle, the heat budget in almost entire body is reduced to the
498 heating from the core by ^{60}Fe decay only and the heating of the mantle from above by the
499 magma ocean. Whereas the melt fraction in the magma ocean is fixed at about 50%, the melt
500 fractions in the deeper regions remain lower (<40%, see Fig. 2 and 4). The effects of the sub-

501 surface magma ocean on the interior temperature wear off after approximately 1 Ma. After
502 this time the temperature profile throughout the mantle establishes a negative gradient from
503 the CMB towards the surface (cooling of the core).

504 For models with $t_0 > 1.0$ Ma almost no melt extrusion at the surface is observed although for
505 $1.0 \leq t_0 < 2.0$ a superheated layer in the sub-surface forms. However, note that we do not
506 consider crust formation via dykes. For $t_0 > 2.0$ Ma the effects of partitioning of ^{26}Al are
507 negligible.

508 Regardless of the formation time, the melt fractions in the silicate mantle of Vesta remain
509 below 40% (except in the shallow magma ocean), either due to the migration of the ^{26}Al
510 enriched melt towards the surface, or as a result of the decline in the radiogenic heating with
511 time. No deep (whole-mantle) magma ocean is observed. Due to the density contrast between
512 the silicate melt and the solid silicate matrix, some melt percolation takes place during the
513 cooling of the depleted mantle. This stops when the temperature decreases below the silicate
514 solidus, e. g., at maximally 150 Ma after the CAIs above the CMB. Silicate melt is present at
515 a depth of 50 km until 28 Ma and at the depth of 100 km until 97 Ma after the CAIs if Vesta
516 forms contemporaneously with the CAIs (see Fig. 2).

517 In the core, as thermal convection takes place only if the heat flow at the CMB surpasses the
518 adiabatic heat flow at the CMB, considerably higher temperatures than the critical
519 temperature for the metal phase of 1456 K resulting in 50% partial melt are attained. Up to
520 75% of the core material manage to melt before convection starts. The temperature profile in
521 the convecting core is regulated by the temperature of the lower mantle directly above the
522 CMB (due to the difference between the potential temperature and the temperature at the
523 upper boundary, which enters the effective thermal conductivity, see Eqn. (5)-(7)). The
524 typical values of the Rayleigh number here are $Ra = O(10^{19})$ and the effective thermal
525 conductivity varies around $O(10^6)$ W m⁻¹ K⁻¹. The cooling through the CMB and the decline in
526 the radiogenic heating puts the outer regions of the core into the advective regime below the

527 RCMF of the metal phase. Subsequently the convecting inner part of the core becomes
528 smaller through freezing of the outer regions until the convection ceases after ≈ 100 Ma after
529 the formation of the body (Note, however, that we do not consider crystal segregation in a Fe-
530 Ni-FeS core – the implications of this process on the results are discussed below).

531 Figure 6 shows the core radius (solid black line), the mantle thickness (dashed line) and the
532 thickness of the undifferentiated outer layer (dotted line) as functions of the formation time.
533 For $t_0 \leq 1.5$ Ma the core radius is approximately 111 km and is smaller for $1.5 < t_0 \leq 2.6$ Ma
534 showing a sharp gradient between 2.3 Ma (97 km) and 2.6 Ma (≈ 1 km). The duration of the
535 differentiation of rather small cores for the latter formation interval amounts to up to 170 Ma
536 (as long as there is any melt). Formation prior to 1.5 Ma results in a complete or almost
537 complete differentiation. At $t_0 = 2.7$ -2.8 Ma no distinct core forms, although some increase in
538 the metal concentration towards the centre can be observed as some melt migration below the
539 radius of 216-188 km, respectively, took place. No melt migration occurred for $t_0 = 2.9$ Ma. As
540 for $t_0 > 2.3$ Ma the solidus temperature of silicates was not exceeded, differentiation for the
541 bodies with later formation time is due to iron melt migration only (and is much slower). For
542 $t_0 \leq 2.3$ Ma a silicate mantle forms and for $t_0 \geq 1.5$ Ma a thin primordial (porous) layer is
543 retained at the surface, thickness of the latter lying between 0.3 km at $t_0 = 1.5$ Ma and 2.8 km at
544 $t_0 = 3$ Ma.

545 The present findings of a shallow magma ocean strongly depend on the migration velocity
546 and here the most critical parameter is the silicate melt viscosity – the higher the viscosity the
547 lower is the migration velocity and the more likely the formation of a global magma ocean
548 and vice versa. In the present model, we have used a silicate melt viscosity of 1 Pas. The
549 viscosity of molten silicates varies from 0.001 to 1000 Pa s (Moskovitz and Gaidos 2011),
550 however, basaltic melts derived from chondritic precursors have silica contents generally \lesssim
551 50% (Mittlefehldt et al. 1998) and viscosities of ≈ 1 -100 Pa s (Giordano et al. 2008). Further
552 tests with melt viscosities of 10 and 100 Pas show that an increase of the silicate melt

553 viscosity results in lower melt migration velocities, thicker sub-surface magma ocean (e.g.
554 ≈ 10 km for 10 Pa s in comparison to 1 km for 1 Pa s) and slower silicate separation. The
555 cooling of the magma ocean below the RCMF is prolonged to 1 Ma and the layer is entirely
556 crystallized after 3 Ma. Higher temperatures are obtained in the mantle and in the core,
557 because of the somewhat prolonged radiogenic heating by the slow migrating ^{26}Al . In the
558 extreme case of 100 Pa s, the magma ocean even extends to the depth of ≈ 100 km. The rest of
559 the mantle reaches melt fractions close to the RCMF and the iron-rich core, the silicate mantle
560 and the crust from almost simultaneously. Apart from the thickness of the sub-surface magma
561 ocean and the melt fractions (temperatures) in the body below, the most important effects
562 described in the general scenario (fast silicate-metal differentiation, extrusion of ^{26}Al , melt
563 fractions in the magma ocean remain close to the threshold of 50%, etc.) are still valid.
564 The amount of heating by ^{60}Fe is connected to the initial ratio $[\text{}^{60}\text{Fe}/\text{}^{56}\text{Fe}]_0 = 1.6 \times 10^{-6}$ adopted
565 in our calculations. To test the influence of this parameter on the results we performed test
566 runs assuming values of 1.0×10^{-7} , 1.0×10^{-8} and 1.0×10^{-9} . The effect on the occurrence and
567 evolution of the magma ocean is negligible, because the abundance of the major heat source
568 ^{26}Al remains constant. Furthermore, the melt fractions in the core and in the lower mantle
569 decrease by less than 10% with the falling initial abundance of ^{60}Fe . This decreases the
570 duration of the thermal convection in the core slightly by less than 10 Ma.
571 In the following, we have also examined the influence of the partitioning of ^{26}Al on the
572 thermo-chemical evolution of Vesta by considering $P=1$ (no partitioning) to better compare
573 the results with models that neglect partitioning. The duration of the differentiation is only
574 slightly shorter than for $P=0.02$, but the order of crust-mantle and core-mantle differentiation
575 differs. As in the case of $P=0.02$, first silicate and iron melt migration is observed at
576 approximately 50 km depth and not in the centre - due to increasing gravity with radius and
577 almost equal melt fraction as in the centre (owed to a flat temperature profile).
578 Simultaneously, the silicate mantle grows down- and upwards from the region where the

579 differentiation started, and the metal core grows upwards from the centre. In the last stage of
580 the iron-silicate differentiation, a clear CMB is established. After core formation, a magma
581 ocean starts to form somewhere in the mid-mantle. The melt from the boundary layer above
582 the magma ocean is not able to percolate through the chondritic carapace and to form a
583 basaltic crust. Even in the hottest scenario with $t_0=0$ Ma an undifferentiated (although
584 compacted) primordial crust of ≈ 1 km thickness remains.

585

586 **4. Discussion and Conclusions**

587 Our simulations imply that no whole-mantle silicate magma ocean formed in the mantle of
588 Vesta – percolation of silicate melt and the depletion of ^{26}Al in the mantle is faster than the
589 heating of the mantle by the radioactive elements, as also suggested by Moskovitz and Gaidos
590 (2011) for smaller bodies. The entire silicate material did not exceed the critical temperature
591 of approximately 1637 K (and the corresponding threshold melt fraction of 50%) and for the
592 most part the melt fractions in the mantle remained below 40%. Even in the thin sub-surface
593 magma ocean this critical temperature is exceeded by only few degrees. The critical
594 temperature varies in general with the assumptions about the melting behavior of the silicate
595 material (we assumed linear melting between the solidus and the liquidus of the silicates).
596 Furthermore, the adopted value of the RCMF of 0.5 can be debated, as liquid-state convection
597 may occur already at lower melt fractions (even values of down to 20% have been suggested,
598 see e. g. Arzi 1978, Taylor 1992, Lejeune and Richet 1995, Scott and Kohlstedt 2006).
599 Assuming a smaller threshold value of the RCMF for the onset of convection would result in
600 the fixation of the temperature in the convecting zone at the temperature corresponding to the
601 associated melt fraction. Thus, the source regions of the melt which formed the HED
602 meteorites most likely never exceeded 20 to 50% melting and the corresponding temperature.

603

604 **Interior evolution of Vesta**

605 Based on our findings we suggest the evolution of the interior of Vesta shown in Fig. 7 a.

606 After the initial accretion phase (which is approximated here by instantaneous formation at

607 the time t_0), the radiogenic heating induces compaction of the porous material and the

608 associated bulk volume decrease. Having a flat temperature profile with a sharp gradient in a

609 thin outer porous layer, melt is produced even in shallow regions. Upon the onset of the

610 differentiation ^{26}Al is enriched in the outer 2-15 km of the body and the high temperatures and

611 high degree of melting close to the surface cause compaction of the chondritic crust, the

612 differentiation of the shallow layers and the melt eruptions at the surface. For viscosities of

613 silicate melt between 1 and 10 Pas a shallow magma ocean with a thickness of 1 to 10 km

614 forms. The magma ocean cools rapidly within $O(10^4)$ - $O(10^6)$ a and its thickness as well as the

615 time scale of solidification increases with increasing silicate melt viscosity.

616 Rapid cooling of the magma ocean on the HED parent body within 2-3 Ma has been

617 suggested as a consequence of ^{26}Mg variations among diogenites and eucrite (Schiller et al.

618 (2011). However, Schiller et al. (2011) concluded that such a rapid cooling can occur only in

619 asteroids with radii smaller than 100 km implying that Vesta is not the parent body of the

620 HEDs. In contrast, our results admit both the size of Vesta and high cooling rates.

621 While ^{26}Al is transported to the surface, the differentiation proceeds downwards: a basaltic

622 crust, a purely silicate upper mantle and an iron-rich core form, with the completion of the

623 mantle and a clear CMB subsequently. The observed basaltic surface of Vesta (e.g., McSween

624 et al., 2013) favours formation times $t_0 < 1$ Ma, as in those cases the silicate melt is able to

625 penetrate the outermost layer via porous flow and thereby to cover the entire surface. This

626 correlates with the lack of a large amount of relict undifferentiated material (e.g., De Sanctis

627 et al. 2012) and the presence of basaltic crust but lack of distinct volcanic regions on Vesta

628 (Jaumann et al. 2012). Volcanism caused by melt transport via dykes may violate these

629 findings. Furthermore, the ^{26}Mg composition of the most primitive diogenites requires onset

630 of the magma ocean crystallization within $0.6_{+0.5}^{-0.4}$ Ma after CAI's (Schiller et al., 2011)
631 consistent with the formation times of $t_0 < 1$ Ma.
632 The silicate-metal differentiation is rapid and in general completed within 0.3 Ma after
633 initiation of melting; nevertheless it succeeds early silicate differentiation. This sequence is
634 different to what is generally assumed for planetesimals from chronological records, i.e., core
635 formation precedes crust formation (e.g., Kleine et al., 2009). To reverse the differentiation
636 sequence either metal segregation needs to be accelerated or silicate segregation slowed
637 down. Metal segregation is enhanced for instance for a high concentration of FeS close to the
638 eutectic (Neumann et al., 2011) or a lower viscosity of iron melt. In the present study, we
639 have assumed a L-chondritic composition of Vesta with only 5 wt% of FeS and a melt
640 viscosity of 10^{-2} Pas. However, higher concentrations of FeS in Vesta have been also
641 suggested with values of ~ 10 wt%, corresponding to a Vesta-like body composed of 70 wt%
642 ordinary chondrite and 30 wt% carbonaceous chondrite (Boesenberg and Delaney, 1997).
643 Furthermore, experiments show a variation of the viscosity of iron-rich melt between 10^{-3} and
644 10^{-2} Pas (Dobson et al., 2000; Assael et al., 2006) and we took the standard value of 10^{-2} Pas
645 used in the literature.

646 Although we cannot discriminate the composition of the various silicate liquid and solid
647 phases in our model, we speculate the first partial melt reaching the surface are non-
648 cumulative eucrites. The cumulative eucrites and the diogenites are suggested to have formed
649 as a consequence of the crystallising sub-surface magma ocean. The latter has an olivine-poor
650 composition as it contains mainly partial melt that is transported upward from the mantle
651 below. In addition, at the same time the original solid matrix in the magma ocean region is
652 pushed down and replaced by crystallising partial melt from the lower mantle. Thus, in our
653 scenario the non-cumulative eucrites form prior to the cumulative eucrites and diogenites.
654 This order of formation is supported by the internal ^{26}Al - ^{26}Mg isochrones obtained by Hublet

655 et al. (2013), who infer younger ages for the diogenites compared to those of the eucrites, and
656 younger ages for the cumulative eucrites compared to the non-cumulative ones.

657 It should be noted, though, that silicate melting and melt migration is ongoing for up to 150
658 Ma and thus much longer than silicate-metal separation. However, the upper melting front
659 moves continuously to greater depth. Partial melting generated later than the early eucritic
660 crust is not able to rise to the surface and will remain in the lower crust or mantle.

661 High values of the silicate melt viscosity between 10 to 100 Pas suggest that the subsurface
662 magma ocean can even reach a thickness up to 100 km. A sub-surface magma ocean with a
663 thickness of a few tens of kilometres would in fact be more consistent with the assumption of
664 Vesta's crust having an average thickness of 35-85 km with an upper eucritic and a lower
665 orthopyroxene-rich layer (McSween et al., 2013).

666 Our results suggest that no global magma ocean down to the core mantle boundary forms
667 because the silicate melt including ^{26}Al is transported toward the surface. This result is in
668 particular valid for a RCMF of 0.5. For smaller values of the critical melt fraction - that
669 determines the change in the rheological behaviour and defines the existence of a magma
670 ocean from the physical perspective (low viscosity) - the critical temperature is reached faster.
671 However, in our approach we have neglected the composition of the various silicate liquid
672 and solid phases and thereby also the variation in the melting temperature with composition.
673 Depleting the mantle in crustal components due to magma migration, results in higher solidus
674 temperatures of the residual material and thus reduced subsequent partial melting in the lower
675 mantle. In contrast, in the shallow magma ocean, which accumulates partial melt of the lower
676 mantle that has a lower liquidus temperature than the primordial material, a higher degree of
677 melting is possible (than calculated in our approach). Thus, a more detailed study that also
678 considers the individual silicate phases may strengthen our finding of a shallow sub-surface
679 and no global magma ocean on Vesta.

680 The iron-rich core starts to convect by thermal buoyancy already during its formation.
681 Convection and cooling of the core through the depleted mantle is then maintained for up to
682 $O(10^8)$ a. It should be noted, though, that the core was - like the mantle - not entirely melted
683 and the melt fraction stayed below 75%. Thus, an early dynamo is not by thermal convection
684 only, i.e. a purely early thermal dynamo is not likely in Vesta. Chemical convection due to
685 freezing processes in the core may play a substantial role for the magnetic field generation in
686 planetesimals (Nimmo, 2009). The freezing process and chemical convection has been
687 simplified in the present study and needs further studies.

688 The less realistic evolution path from Fig. 7 b results in the formation of a convecting whole-
689 mantle magma ocean. Here, the distribution of ^{26}Al is homogeneous throughout the silicate
690 phase (both solid and liquid). Note that by contrast to previous thermo-chemical evolution
691 models considering a magma ocean scenario (e.g. Gupta and Sahijpal, 2010), the
692 differentiation does not start in the centre, but in the upper mantle. Furthermore, the silicate
693 melt from the mantle is not able to penetrate the chondritic crust via porous flow, thus likely
694 no basalts form at the surface and the differentiation is not complete. However, ongoing
695 impacts, presence of volatiles, and excess pressure in the interior due to melting could act in
696 favour of melt ascent via cracks to produce a basaltic crust (Wilson and Keil, 2012). The
697 chondritic crust could be also carved off by impacts exposing the differentiated silicate layers
698 although one would expect relicts of undifferentiated material that have not been observed
699 (e.g., De Sanctis et al. 2012).

700

701 **Comparison to previous thermo-chemical evolution models**

702 Our results suggest that most previous thermo-chemical evolution models for Vesta tend to
703 overestimate the temperature increase in the interior and therefore the amount of partial
704 melting (Righter and Drake 1997, Ghosh and McSween 1998, Drake 2001, Gupta and

705 Sahijpal 2010). Those models either neglect efficient heat transport by the partitioning of ^{26}Al
706 into the silicate melt or convection in a magma ocean.

707 The convective cooling method used by Hevey and Sanders (2006) for small planetesimals <
708 100 km in radius (increase of k by three orders of magnitude for melt fractions $\geq 50\%$) has
709 been also adopted by Gupta and Sahijpal (2010) for Vesta (a steady increase of the thermal
710 diffusivity between the melt fractions of 50% and 100% by three orders of magnitude).

711 Thus, a maximal value of $\approx 3300 \text{ W m}^{-1} \text{ K}^{-1}$ has been used for effective thermal conductivity
712 by Gupta and Sahijpal (2010). The effective thermal conductivity, however, varies with the
713 cube root of gravity times the depth of the convecting zone (Eqn. (5) - (7)). Hence, the larger
714 the radius and / or the convecting zone, the larger is k_{eff} . In our simulations values of $O(10^6)$
715 $\text{W m}^{-1} \text{ K}^{-1}$ can be obtained for $\Delta T = O(1) \text{ K}$ (the difference between the potential temperature
716 and the temperature at the upper boundary of the convecting zone. This explains the much
717 higher temperatures of up to 2000 K obtained by Gupta and Sahijpal (2010). Our model in
718 which the partitioning of ^{26}Al is neglected as in Gupta and Sahijpal (2010) show a global
719 magma ocean but still the temperatures do not exceed significantly the threshold melt fraction
720 of 50% due to efficient cooling.

721 Our results further imply that previous thermal evolution models for planetesimals to explain
722 the magnetic field generation in their iron-rich cores such as presented in e. g. Elkins-Tanton
723 et al. (2011), Elkins-Tanton (2012) and Sterenborg and Crowley (2013) have to be considered
724 with care although they consider efficient cooling by convection. These models start with a
725 differentiated structure and further neglect volcanic heat transport and partitioning of ^{26}Al .

726 Thereby, thermal convection in the core and magnetic field generation is initiated due the
727 efficient cooling of the magma ocean after an initial phase of heating by the radioactive heat
728 sources. It can be shown in our models that when considering the entire differentiation
729 process, i.e. silicate-metal and silicate-silicate differentiation, that the temperature profile after
730 core formation shows a temperature profile increasing toward the surface and inhibiting

731 convection. A whole-mantle magma ocean does not form and, as a consequence, the lower
732 mantle cools by conduction only. Nevertheless, the core heat flow is higher than the heat flow
733 along the core adiabat suggesting thermal convection in the core for about 100 Ma. This
734 finding is in contrast to the assumption of Sterenborg and Crowley (2013), who argue that
735 thermal convection in the core is inhibited when the mantle cools by conduction using a
736 simple model of conductive cooling. It should be noted though that the strength of thermal
737 core convection in our model is likely not sufficiently strong to generate a dynamo, i.e. if the
738 magnetic Reynolds number is lower than about $O(10-100)$ (e.g., Christensen et al., 1999).
739 However, we do not explicitly differentiate between the iron-nickel system and lighter
740 elements in the core (such as those contained in the Fe-FeS system). This means that our
741 model does not allow freezing and growth of a solid inner core and the establishment of a
742 liquid outer core due to the exclusion of light elements from the crystal structure, as well as
743 the latent heat release at the inner core boundary. Thus, chemically driven convection
744 (Stevenson 2003; Nimmo, 2009) and its contribution to the magnetic field are neglected.

745

746 **Solid-state convection**

747 As mentioned further above, the solid-state plastic deformation (other than compaction due to
748 sintering, see e.g. Tkalcic et al. 2013) for melt fractions below 50% has been neglected in the
749 present study. First, the conditions for solid-state convection are fulfilled several million years
750 after the solidification of the shallow magma ocean. Before that time, the temperatures in the
751 upper mantle (magma ocean region) are higher than in the lower mantle and thermal
752 convection is suppressed. Second, the maximal Rayleigh number that we obtain when the
753 conditions are favourable for convection is estimated to be ≈ 5500 , which exceeds the critical
754 Rayleigh number of 1000 (e.g. Schubert et al. 2001) required for convection only moderately.
755 Because this type of convection takes place after the magma ocean has vanished, it has no
756 effect on the main results presented in the paper. However, the latest time of occurrence of

757 partial melt in the mantle and the time scale of the convection in the core could change
758 slightly.

759

760 **Melt ascent through a porous crust and formation of dykes**

761 Our results suggest the formation of a basaltic crust by porous flow. It has been argued
762 however, that melt ascent through a porous chondritic crust is unlikely due to the lack of the
763 positive density contrast (e.g. Elkins-Tanton et al. 2011). In our simulations of Vesta the
764 porous chondritic material compacts readily due to hot pressing if exposed to the temperatures
765 far below the silicate solidus of ≈ 1425 K. Consequently, the density contrast between the melt
766 and the matrix is still maintained. This result is supported by the numerical simulations of
767 Henke et al. (2012, 2013). When the silicate melt reaches the porous layer, this layer has
768 already been exposed to temperatures high enough to compact (and compacted in the course
769 of a self-consistent calculation). Eventually, an extremely thin surface shell (~ 100 m thick)
770 remains porous which does not represent a barrier for buoyant rising melt (see Fig. 6 and
771 discussion on grid resolution in the Supplementary Material). On the other hand, compacted
772 chondritic material at the surface could have been fractured due to impacts. However, this
773 should not hinder melt ascension, but would rather favour the extraction of melt via dykes.
774 Also, large pressures can be generated in the sub-surface for small degrees of melting (e. g. a
775 pressure of 0.1 GPa for a melt fraction of 0.2, see Wilson and Keil, 2012), and eruptions
776 would occur when the excess pressure due to the accumulation of magma in the sub-regolith
777 reservoirs exceeds the tensile stress of the overlying rock (Wilson and Keil, 2012). The
778 presence of small amounts of volatiles reduces the magma density and increases even the
779 excess pressure. Note, though, that to keep the fractures open and to allow efficient cooling by
780 the silicate melt transport directly from the deep mantle to the surface, Vesta may be a
781 boundary case due to its small size. Instead, magma would first accumulate in sills or magma

782 layers at the base of the upper thermal boundary layer before eruption (Wilson and Keil,
783 2012).

784 Efficient melt migration via dykes – if possible - suggests even faster cooling of the interior
785 than via porous flow and even strengthens the result presented here. Consequently, faster
786 cooling of the mantle and a shorter time span of the convection in the core are expected.

787

788

789

790

791

792

793

794

795

796

797

798

799

800

801

802

803

804

805

806

807

808 **References**

- 809 Arzi, A. A., 1978. Critical phenomena in the rheology of partially melted rocks.
810 *Tectonophysics* 44, Issues 1-4, 173-184.
- 811 Asmar, S. W., 9 colleagues, 2012. The gravity field of Vesta and implications for interior
812 structure. *Lunar and Planetary Science XLIII*, 2600 (abstract).
- 813 Asphaug, E., 1997. Impact origin of the Vesta family. *Meteoritics and Planetary Science* 32,
814 965-980.
- 815 Assael, M. J., 10 colleagues, 2006. Reference data for the density and viscosity of liquid
816 aluminum and liquid iron. *Journal of physical and chemical reference data* 35, 285.
- 817 Barrat J.A, Yamaguchi A., Benoit M., Cotten J., Bohn M., 2008. Geochemistry of diogenites :
818 Still more diversity in their parental melts. *Meteoritics & Planetary Science* 43, Issue 11,
819 1759-1775.
- 820 Beck, A. W., McSween, H. Y., 2010. Diogenites as polymict breccias composed of
821 orthopyroxenite and harzburgite. *Meteoritics & Planetary Science* 45, Issue 5, 850-872.
- 822 Best, M. G., 2002. *Igneous and Metamorphic Petrology*, 2nd Edition. Wiley-Blackwell, 2002.
- 823 Boesenberg, J.S. and Delaney, J.S., A model composition of the basaltic achondrite planetoid.
824 *Geochimica et Cosmochimica Acta* 61, 3205-3225, 1997.
- 825 Cameron A.G.W., 1993. Nucleosynthesis and star formation. In: Levy, E. H., Lunine, J. I.
826 (Eds.), *Protostars and Planets III*, Univ. of Arizona Press, Tucson, p. 47.
- 827 Christensen, U., Olson, P., Glatzmaier, G.A., 2009. Numerical modeling of the geodynamo: A
828 systematic parameter study. *Geophysical Journal International* 138, 393-409.

829 Delaney, J. S., 1995. 4 Vesta: A thick-skinned parent for basaltic achondrites. *Lunar and*
830 *Planetary Science XXVI*, 329-330 (abstract).

831 De Sanctis, M. C., 22 colleagues, 2012. Spectroscopic Characterization of Mineralogy and Its
832 Diversity Across Vesta. *Science* 336, 697.

833 De Sanctis, M. C., 17 colleagues and Dawn Team, 2013. Olivine on Vesta: clues for the
834 interior. *European Planetary Science Congress 2013, EPSC2013-437* (abstract).

835 Dobson, D., P., 8 colleagues, 2000. In situ measurement of viscosity of liquids in the Fe-FeS
836 system at high pressures and temperatures. *American Mineralogist* 85, 11-12, 1838-1842.

837 Drake, M. J., 2001. The eucrite/Vesta story. *Meteoritics & Planetary Science* 36 (4), 501–513.

838 Elkins-Tanton, L. T., Weiss, B. P., Zuber, M. T., 2011. Chondrites as samples of
839 differentiated planetesimals. *Earth and planetary science letters* 305, 1-10.

840 Elkins-Tanton, L. T., 2012. Magma oceans in the inner solar system. *Annual review of Earth*
841 *and planetary sciences* 40, 113-139.

842 Fu, R. R., and 7 colleagues, 2012a. An ancient core dynamo in asteroid Vesta. *Science* 338,
843 238-241.

844 Fu, R. R., Weiss, B. P., Li, L., Suavet, C., Gattacceca, J., Lima, E. A., 2012b. Magnetic fields
845 on 4 Vesta as recorded in two eucrites. *Lunar and Planetary Science XLIII*, 1496 (abstract).

846 Ghosh, A., McSween, H. Y. Jr., 1998. A Thermal Model for the Differentiation of Asteroid 4
847 Vesta, Based on Radiogenic Heating. *Icarus* 134, 187-206.

848 Giordano, D., Russell, J. K., Dingwell, D. B., 2008. Viscosity of magmatic liquids: A model.
849 *Earth and Planetary Science Letters* 271, 123–134.

850 Golabek, G. J., Keller, T., Gerya, T. V., Zhu, G., Tackley, P. J., Connolly, J. A. D., 2011.
851 Origin of the Martian dichotomy and Tharsis from a giant impact causing massive
852 magmatism. *Icarus* 215, 346-357.

853 Gupta, G., Sahijpal, S., 2010. Differentiation of Vesta and the parent bodies of other
854 achondrites. *Journal of geophysical research* 115, E08001.

855 Greenwood, R. C., Franchi, I. A., Jambon, A., Buchanan, P. C., 2005. Widespread magma
856 oceans on asteroidal bodies in the early Solar System. *Nature* 435, 916-918.

857 Hevey, P. J., Sanders, I. S., 2006. A model for planetesimal meltdown by ^{26}Al and its
858 implications for meteorite parent bodies. *Meteoritics & Planetary Science* 41, 95-106.

859 Hublet G., Debaille V., Wimpenny J., Yin Q.-Z., 2013. Geological History of 4-Vesta: ^{26}Al -
860 ^{26}Mg Dating on Eucrites and Diogenites. *Mineralogical Magazine*, 77(5), 1343.

861 Ikeda, Y., Takeda, H., 1985. A model for the origin of basaltic achondrites based on the
862 Yamato 7308 howardite. *Journal of Geophysical Research* 90, C649-C663.

863 Ivanov, B. A., Melosh, H. J., 2013. Two-dimensional numerical modeling of the Rheasilvia
864 impact formation. *Journal of Geophysical Research: Planets* 118, Issue 7, 1545-1557.

865 Jarosevich, E., 1990. Chemical analyses of meteorites: A compilation of stony and iron
866 meteorite analyses. *Meteoritics* 25, 323-337.

867 Jaumann, R., 42 colleagues, 2012. Vesta's shape and morphology. *Science* 336, 6082, 687.

868 Jutzi, M., Asphaug, E., 2011. Mega-ejecta on asteroid Vesta. *Geophysical Research Letters*
869 38, L01102.

870 Kennedy, A., Lofgren, G., Wasserburg, G., 1993. An experimental study of trace element
871 partitioning between olivine, orthopyroxene, and melt in chondrules: equilibrium values and
872 kinetic effects. *Earth and Planetary Science Letters* 115, 177-195.

873 Kleine T., 8 colleagues, 2009. Hf-W chronology of the accretion and early evolution of
874 asteroids and terrestrial planets. *Geochimica et cosmochimica acta* 73, Nr. 17, 5150-5188.

875 Kraichnan, R. H., 1962. Turbulent thermal convection at arbitrary Prandtl number. *The*
876 *physics of fluids* 5, 11, 1374-1389.

877 Lejeune, A.-M., Richet, P., 1995. Rheology of crystal-bearing silicate melts: An experimental
878 study at high viscosities. *Journal of geophysical research: Solid Earth (1978-2012)* 100, B3,
879 4215-4229.

880 Mandler, B. E., and Elkins-Tanton, L. T. 2013. The origin of eucrites, diogenites, and olivine
881 diogenites: Magma ocean crystallization and shallow magma chamber processes on Vesta.
882 *Meteoritics & Planetary Science*, DOI: 10.1111/maps.12135

883 Marchi, S., 11 colleagues, 2012. The violent collisional history of asteroid 4 Vesta. *Science*
884 336, 690-694.

885 Marsh, B. D., 1988. Crystal capture, sorting, and retention in convecting magma. *Geological*
886 *Society of America Bulletin* 100, 11, 1720-1737.

887 McSween, H. Y., 21 colleagues, 2013. Composition of the Rheasilvia basin, a window into
888 Vesta's interior. *Journal of Geophysical Research: Planets*, 118, 2, 335-346.

889 Mittlefehldt D., McCoy, T., Goodrich, C., Kracher, A., 1998. Non-chondritic meteorites from
890 asteroidal bodies. In: *Planetary materials*, Papike J. (Ed.), *Reviews in Mineralogy*, vol. 36,
891 Washington, D.C., Mineralogical Society of America, 4.01–4.195.

892 Neumann, W., Breuer, D., Spohn, T., 2012. Differentiation and core formation in accreting
893 planetesimals. *Astronomy and Astrophysics* 543, A141, 1-21.

894 Neumann, W., Breuer, D., Spohn, T., 2013. The thermo-chemical evolution of asteroid 21
895 Lutetia. *Icarus* 224, 126-143.

896 Nimmo, F., 2009. Energetics of asteroid dynamos and the role of compositional convection.
897 *Geophysical Research Letters* 36, L10201.

898

899 Ogliore R. C., Huss G. R., and Nagashima K. 2011. Ratio estimation in SIMS analysis.
900 *Nuclear Instruments and Methods, Physics Research B: Beam Interactions with Materials and*
901 *Atoms* 269, 1910–1918.

902 Pack, A., Palme, H., 2003. Partitioning of Ca and Al between forsterite and silicate melt in
903 dynamic systems with implications for the origin of Ca, Al-rich forsterites in primitive
904 meteorites. *Meteoritics & Planetary Science* 38, 1263-1281.

905 Palme H., Rammensee W., 1981. The cosmic abundance of molybdenum. *Earth and Planetary*
906 *Science Letters* 55, 356-362.

907 Prettyman, T. H., 19 colleagues, 2012. Elemental mapping by Dawn reveals exogenic H in
908 Vesta's regolith. *Science* 338, 242-246.

909 Raymond, C. A., 9 colleagues, 2012. Geophysical exploration of Vesta. *Lunar and Planetary*
910 *Science* XLIII, 1007 (abstract).

911 Reddy, V., 26 colleagues, 2012. Color and Albedo Heterogeneity of Vesta from Dawn.
912 *Science* 336, 700.

913 Rivoldini, A., Van Hoolst, T., Verhoeven, O., Mocquet, A., Dehant, V., 2011. Geodesy
914 constraints on the interior structure and composition of Mars. *Icarus* 213, 451-472.

915 Ruesch, O., 14 colleagues, 2013. Seeing through the pyroxene: distribution of olivine-bearing
916 material on Vesta using VIR/Dawn data. European Planetary Science Congress 2013,
917 EPSC2013-891 (abstract).

918 Russell, C. T., 23 colleagues, 2013. Dawn completes its mission at 4 Vesta. *Meteoritics &*
919 *Planetary Science*, 1–14.

920 Righter, K., Drake, M. J., 1997. A magma ocean on Vesta: Core formation and petrogenesis
921 of eucrites and diogenites. *Meteoritics & Planetary Science* 32 (6), 929–944.

922 Rugel, G., 9 colleagues, 2009. New measurement of the ^{60}Fe half-life. *Physical review letters*
923 103 (7): 072502.

924 Russell, C. T., 27 colleagues, 2012. Dawn at Vesta: Testing the Protoplanetary Paradigm.
925 *Science* 336, 6082, 684.

926 Ruzicka, A., Snyder, G. A., Taylor, L. A., 1997. Vesta as the howardite, eucrite and diogenite
927 parent body: Implications for the size of a core and for large-scale differentiation. *Meteoritics*
928 *& Planetary Science* 32, 825-840.

929 Samuel, H., 2012. A re-evaluation of metal diapir breakup and equilibration in terrestrial
930 magma oceans. *Earth and Planetary Science Letters* 313-314, 105-114.

931 Schenk, P., 11 colleagues, 2012. Mega-impacts into planetary bodies; global effects of the
932 giant Rheasilvia impact basin on Vesta. *Lunar and Planetary Science XLIII*, 2757 (abstract).

933 Schiller, M., Baker, J., Creech, J., Paton, C., Mullet, M.-A., Irving, A., Bizzarro, M., 2011.
934 Rapid timescales for magma ocean crystallization on the howardite-eucrite-diogenite parent
935 body. *The Astrophysical Journal Letters* 740, L22, 6pp.

936 Schubert, G., Turcotte, D. L., Olson, P., 2001. *Mantle Convection in the Earth and Planets*.
937 Cambridge University Press, 940pp.

938 Scott, T., Kohlstedt, D.L., 2006. The effect of large melt fraction on the deformation behavior
939 of peridotite. *Earth and Planetary Science Letters* 246, 177–187.

940 Shearer, C. K., Fowler, G. W., Papike, J. J., 1997. Petrogenetic models for the origin of
941 diogenites and their relationship to basaltic magmatism on the HED parent body. *Meteoritics*
942 *and Planetary Science* 32, 877-889.

943 Siggia, E. D., 1994. High Rayleigh number convection. *Annual Review of Fluid Mechanics*
944 26, 137-168.

945 Sohl, F., Spohn, T., 1997. The interior structure of Mars: Implications from SNC meteorites.
946 *Journal of Geophysical Research: Planets* (1991–2012), 102, E1, 1613–1635.

947 Solomatov, V. S., 2007. Magma oceans and primordial mantle differentiation. In: *Treatise on*
948 *Geophysics*, G. Schubert (ed.), Elsevier, 9, pp. 91-120.

949 Sterenborg, M. G, Crowley J. W., 2013. Thermal evolution of early solar system
950 planetesimals and the possibility of sustained dynamos. *Physics of the Earth and Planetary*
951 *Interiors* 214, 53-73.

952 Stevenson, D. J., 2003. Planetary magnetic fields. *Earth and planetary science letters* 208, 1-
953 11.

954 Stolper, E., 1975. Petrogenesis of eucrite, howardite and diogenite meteorites. *Nature* 258,
955 220-222.

956 Stolper, E., 1977. Experimental petrology of eucrite meteorites. *Geochimica and*
957 *Cosmochimica Acta* 41, 587-611.

958 Takeda, H., 1997. Mineralogical records of early planetary processes on the howardite,
959 eucrite, diogenite parent body with reference to Vesta. *Meteoritics & Planetary Science* 32,
960 841-853.

961 Taylor, G. J., 1992. Core formation in asteroids. *Journal of geophysical research: Planets*
962 (1991-2012) 97, E9, 14717-14726.

963 Telus M., Huss G. R., Oglione R. C., Nagashima K., Tachibana S., 2012. Recalculation of
964 data for short-lived radionuclide systems using less-biased ratio estimation. *Meteoritics &*
965 *Planetary Science* 47, 2013-2030.

966 Tkalcec, B. J., Golabek, G. J., Brenker, F. E., 2013. Solid-state plastic deformation in the
967 dynamic interior of a differentiated asteroid. *Nature Geoscience* 6, 93-97.

968 Warren, P. H., 1985. The magma ocean concept and lunar evolution. *Annual review of the*
969 *Earth and planetary science* 13, 201-240.

970 Warren, P. H., 1997. Magnesium oxide-iron oxide mass balance constraints and a more
971 detailed model for the relationship between eucrites and diogenites. *Meteoritics & Planetary*
972 *Science* 32, 945-963.

973 Wilson, L., Keil, K., 2012. Volcanic activity on differentiated asteroids: A review and
974 analysis. *Chemie der Erde* 72, 289-321.

975 Yomogida, K., Matsui, T., 1983. Physical properties of ordinary chondrites. Journal of
976 Geophysical Research 88, 9513-9533.

977 Zellner, B. J. et al., 1997. Hubble Space Telescope Images of Asteroid Vesta in 1994. Icarus
978 128 (1), 83.

979

980

981

982

983

984

985

986

987

988

989

990

991

992

993 **Figure captions**

994 Fig. 1. Occurrence of iron and / or silicate melt for different formation times of Vesta
995 assuming heat transport by conduction only and no differentiation.

996 Fig. 2. Temporal evolution of the radial distribution of the interior temperature in K (left
997 column) and melt fraction (right column) for different formation times relative to the CAIs.
998 The panels correspond from top to bottom to $t_0=0$, 1, 2, and 2.3 Ma.

999 Fig. 3. Temperature (in K) and two close-ups in the sub-surface magma ocean of a body which
1000 formed at $t_0=0.5$ Ma after the CAIs.

1001 Fig. 4. Melt fraction and two close-ups in the sub-surface magma ocean of a body which
1002 formed at $t_0=0.5$ Ma after the CAIs.

1003 Fig. 5. Close-ups of the sub-surface magma ocean or the super-heated sub-surface region for
1004 different formation times: $t_0=0$ Ma (upper panels), 1 Ma (middle panels), 2 Ma (lower panels).
1005 Left column: Temperature is in K. Right column: Melt fraction.

1006 Fig. 6. Left panel: Density versus depth for different formation times after the cooling below
1007 the solidus temperature of the metal phase. Right panel: Core radius, mantle thickness and the
1008 thickness of the undifferentiated layer for different formation times. Note that for $t_0 \geq 2.3$ Ma
1009 no clear mantle forms.

1010 Fig. 7. **a** Evolution path of the interior assuming partitioning of ^{26}Al . **b** Evolution path of the
1011 interior neglecting partitioning of ^{26}Al .

1012

1013

1014

1015

1016 **Tables**1017 **Table 1.** Composition, density and thermal conductivity.

Phase	Mineral	Mass fraction [%]	Volume fraction [%]	ρ_{solid} [kg m ⁻³]	ρ_{liquid} [kg m ⁻³]	k [W m ⁻¹ K ⁻¹]
Metal	-	14	7.79	6471.12	5490.88	10.2
	Fe	8	-	7874	6980.00	21
	Ni	1	-	8908	7810.00	21
	FeS	5	-	4830	3920.00	4.6
Silicates	-	86	92.21	3357.55	2900	3.8
	Olivine	49	-	3510.00	-	4.3
	orthopyroxene	23	-	3380.00	-	3.9
	clinopyroxene	6	-	3320.00	-	4.6
	Plagioclase	8	-	2630.00	-	1.9
Total	L-chondrite	100	100	3600.05	3105.12	4.2

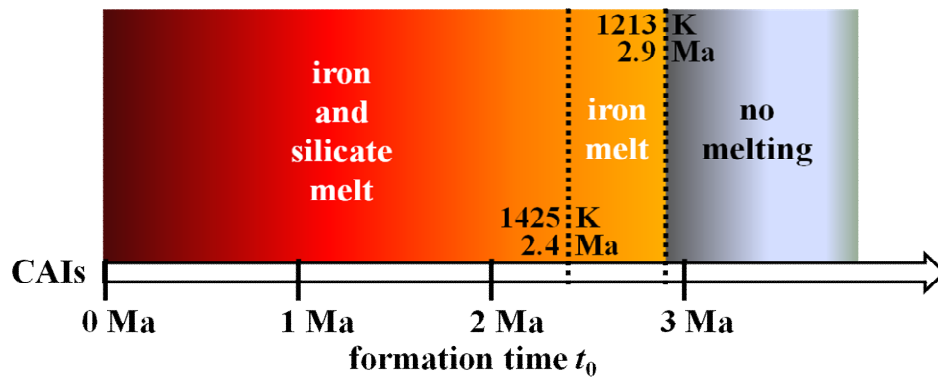
1018 This data is for the most part from Yomogida and Matsui 1983 for L-chondrites.

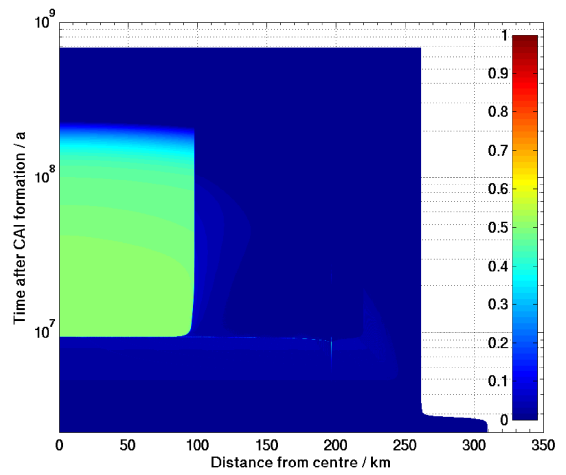
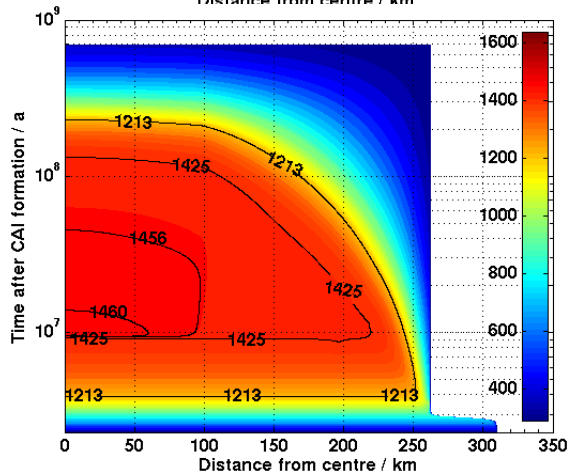
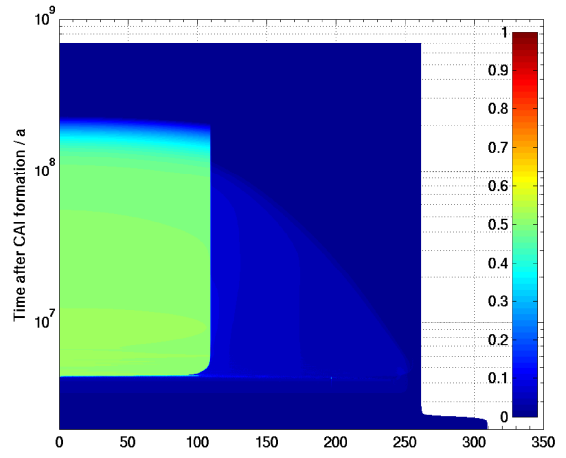
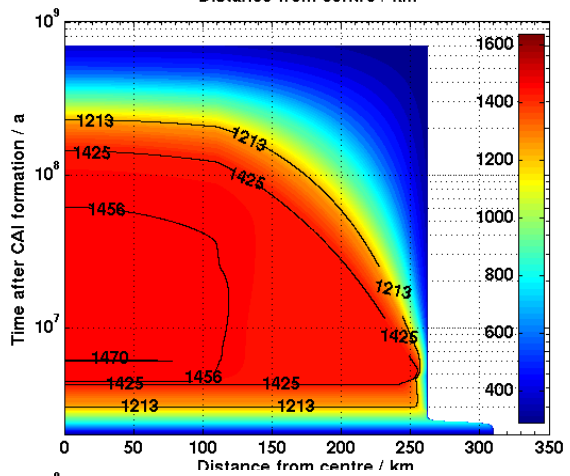
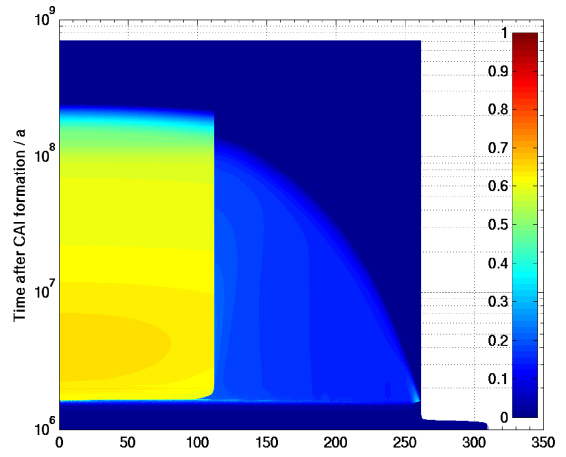
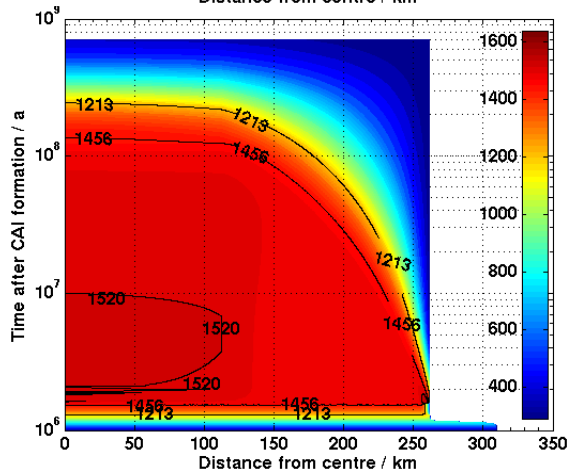
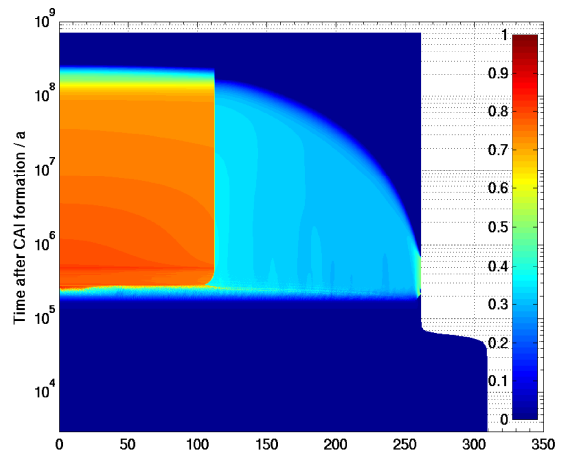
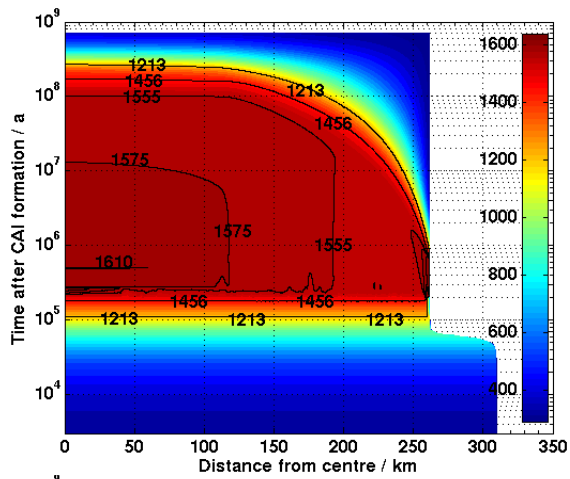
1019 **Table 2.** Parameter values used for the models.

Quantity	Symbol	Unit	Value	Reference
Initial porosity	ϕ_0	-	0.4	1
Reference radius	D	Km	262	2
Initial radius	R_p	Km	310	2
Thermal expansivity of iron	α_{Fe}	K ⁻¹	7.70×10^{-5}	3
Thermal expansivity of silicates	α_{Si}	K ⁻¹	2.00×10^{-5}	4
Iron melt viscosity	$\eta_{l,\text{Fe}}$	Pa s	10^{-2}	1
Silicate melt viscosity	$\eta_{l,\text{Si}}$	Pa s	1	1
Metal solidus temperature	$T_{S,\text{Fe}}$	K	1213	1
Metal liquidus temperature	$T_{L,\text{Fe}}$	K	1700	1
Silicate solidus temperature	$T_{S,\text{Si}}$	K	1425	1
Silicate liquidus temperature	$T_{L,\text{Si}}$	K	1850	1
Radius of iron globules	b	M	0.01	2
Partitioning coefficient	P	-	0.02	1
Stefan-Boltzmann constant	σ_{SB}	W m ⁻² K ⁻⁴	5.67×10^{-8}	-
Emissivity	E	-	0.8	5
Avogadro number	N_A	mol ⁻¹	6.02×10^{23}	-
Nebula temperature	T_N	K	290	1
Decay energy per atom of ²⁶ Al	$E_{26\text{Al}}$	J	$6.41 \cdot 10^{-13}$	1
Decay energy per atom of ⁶⁰ Fe	$E_{60\text{Fe}}$	J	$4.87 \cdot 10^{-13}$	1
Initial abundance of ²⁶ Al	$f_{26\text{Al}}$	kg ⁻¹	$2.76 \cdot 10^{23}$	2
Initial abundance of ⁶⁰ Fe	$f_{60\text{Fe}}$	kg ⁻¹	$1.12 \cdot 10^{24}$	2
Mass fraction of bulk Al	m_{Al}	%	1.19	2
Mass fraction of bulk Fe	m_{Fe}	%	11.18	2
Initial ratio of ²⁶ Al	$[\text{}^{26}\text{Al}/\text{}^{27}\text{Al}]_0$	-	$5 \cdot 10^{-5}$	1
Initial ratio of ⁶⁰ Fe	$[\text{}^{60}\text{Fe}/\text{}^{56}\text{Fe}]_0$	-	$1.6 \cdot 10^{-6}$	1
Half-life of ²⁶ Al	$\tau_{1/2}(\text{}^{26}\text{Al})$	Ma	0.717	1
Half-life of ⁶⁰ Fe	$\tau_{1/2}(\text{}^{60}\text{Fe})$	Ma	2.61	6

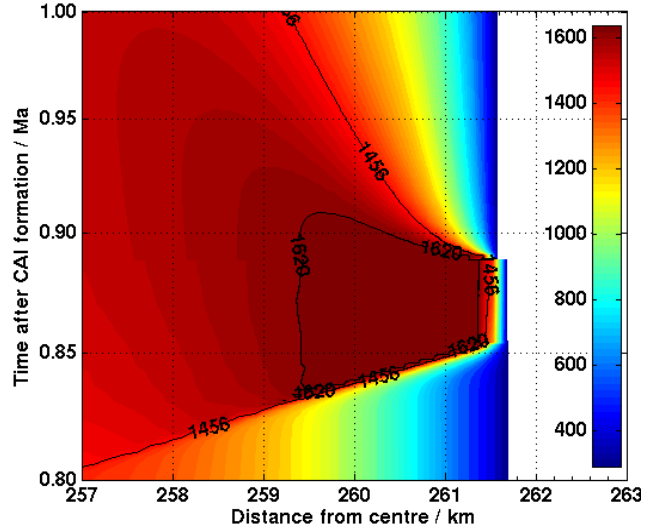
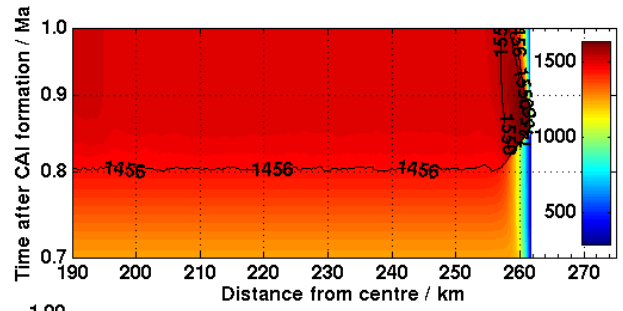
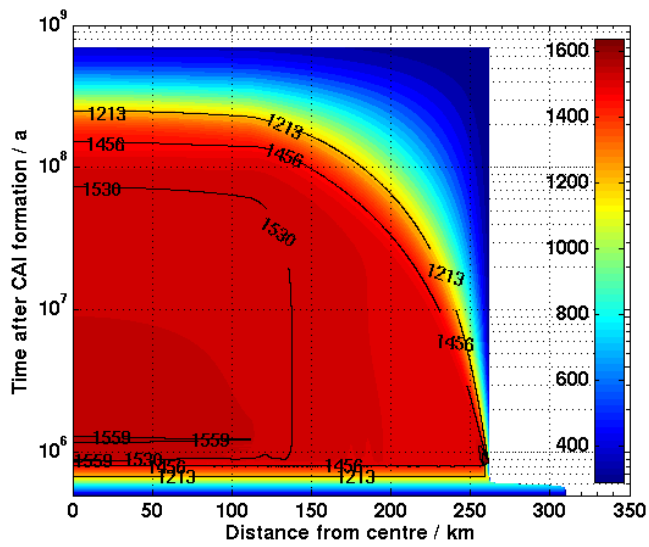
1020 **References:** 1 Neumann et al. 2012. 2 Model section. 3 Rivoldini et al. 2011. 4 Sohl and Spohn 1997. 5
1021 Ghosh and McSween 1998. 6 Rugel et al. (2009)

1022 **Figures**





1035 Fig. 2.

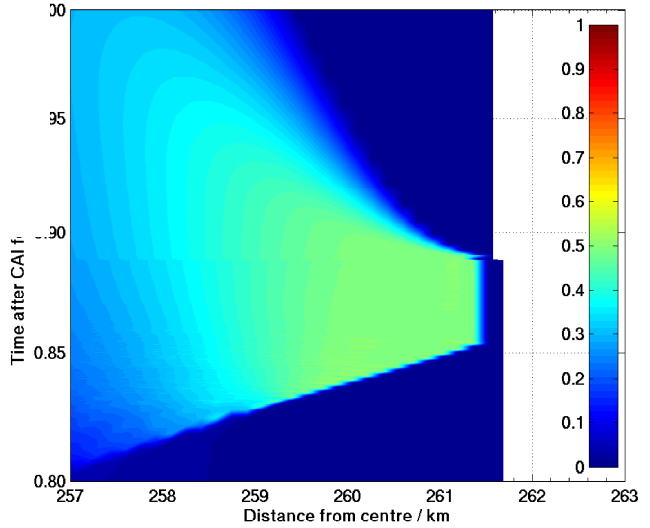
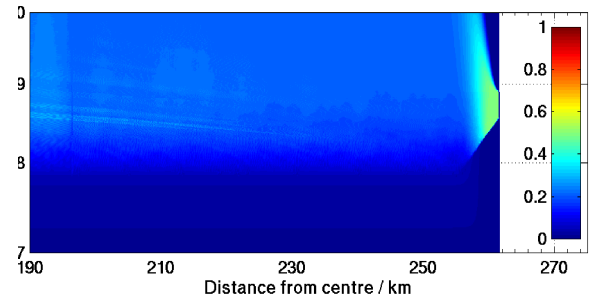
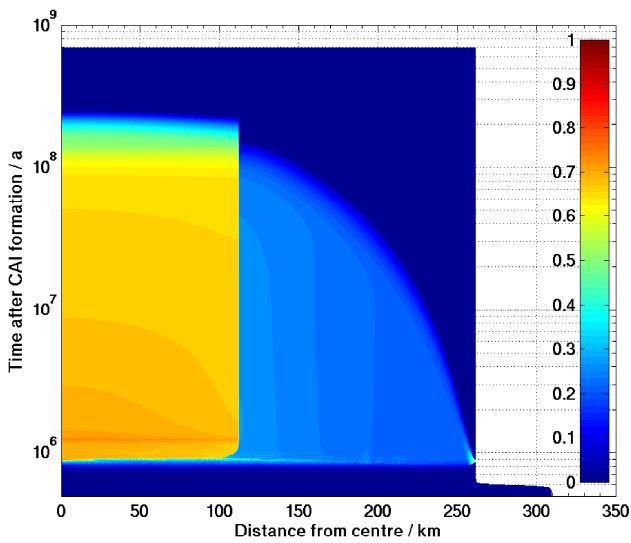


1036

1037

1038

1039 **Fig. 3.**



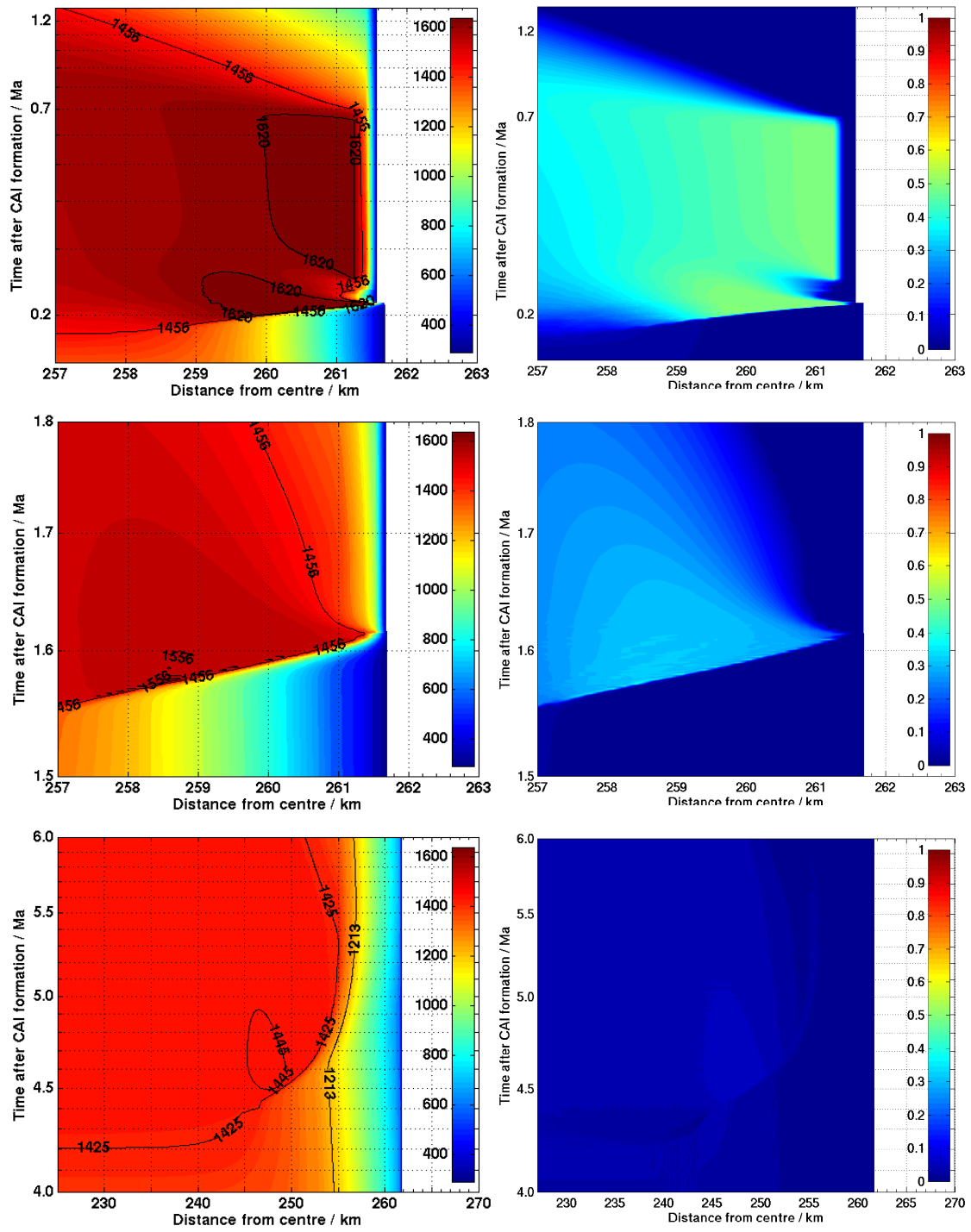
1040

1041

1042

1043 **Fig. 4.**

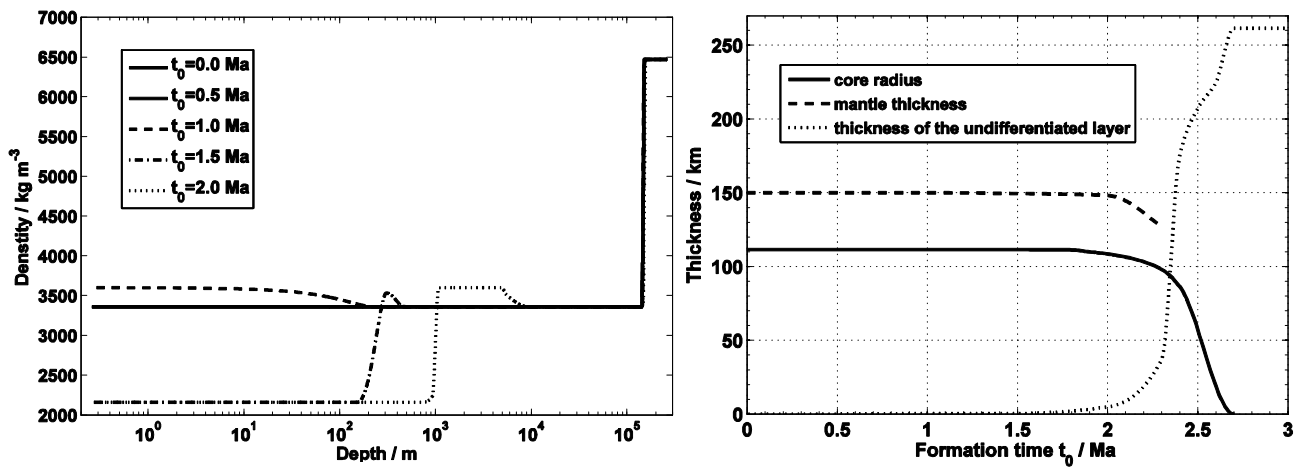
1044



1045 **Fig. 5.**

1046

1047



1048

1049 **Fig. 6.**

1050

1051

1052

1053

1054

1055

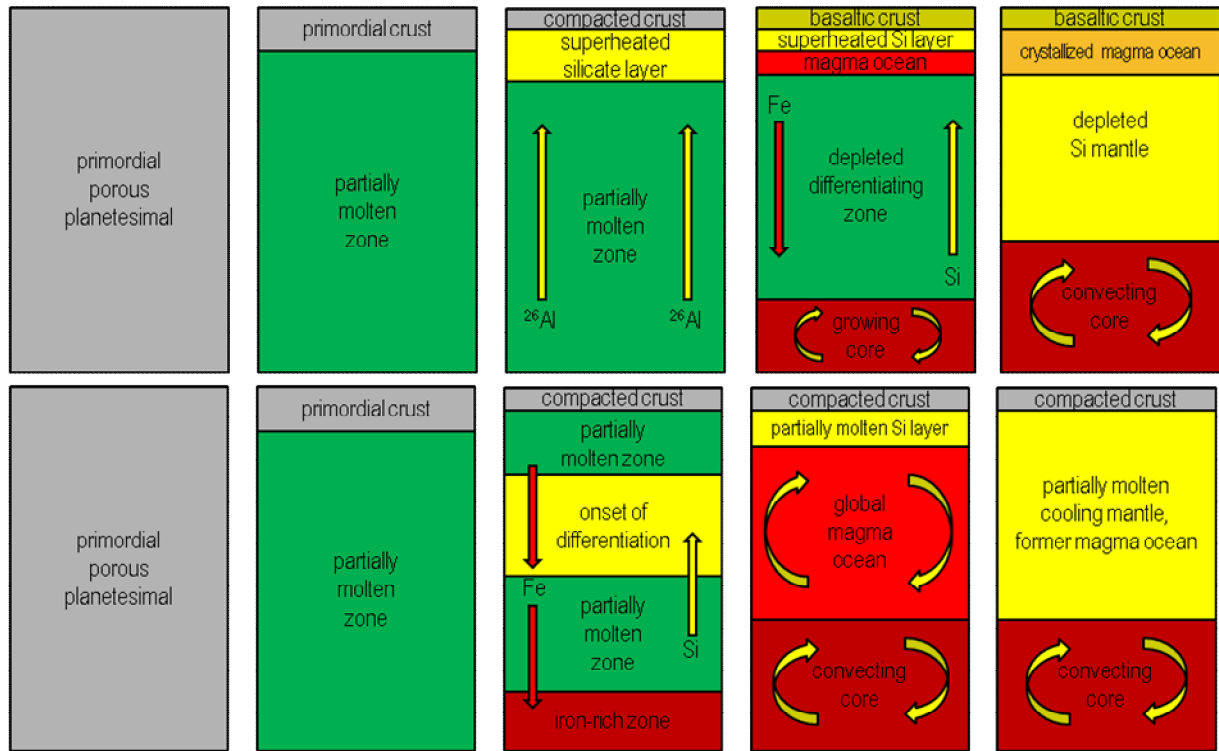
1056

1057

1058

1059

1060



1061

1062 **Fig. 7.**

1 Supplementary material

2 Benchmark tests

3 In the following we will show tests of our numerical approach against existing models in the
4 literature. It should be noted, however, that there are not many codes which consider
5 additional processes apart from conduction in planetesimals. Among those, only a few are
6 available or are documented well enough for us to be able to recalculate some of the results.
7 Furthermore, in most cases the processes like melting, consumption and release of latent heat,
8 and differentiation are treated in a completely different manner. We compare heat conduction
9 (Miyamoto et al. 1981, Šrámek et al. 2012), melting and latent heat consumption and release
10 (Moskovitz 2011, Merk 2002), and differentiation (Šrámek et al. 2012).

11 1 Miyamoto et al. (1981) (conduction only)

12 Parameters for an H-chondrite adopted by Miyamoto (1981):

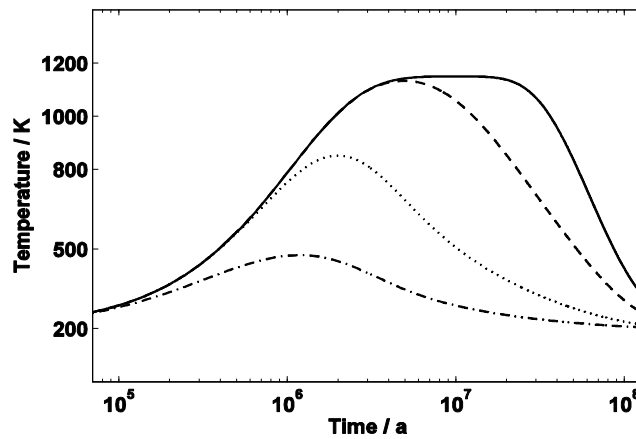
13	Radius	R	85	km
14	Formation time rel. to CAIs	t_0	0	Ma
15	Thermal conductivity	k	1	$\text{W m}^{-1} \text{K}^{-1}$
16	Density	ρ	3200	kg m^{-3}
17	Specific heat capacity	c_p	625	$\text{J kg}^{-1} \text{K}^{-1}$
18	Initial / surface temperature	T_0, T_N	200	K
19	Porosity	ϕ	0	-
20	Initial ratio $^{26}\text{Al}/^{27}\text{Al}$	$[^{26}\text{Al}/^{27}\text{Al}]_0$	5.0×10^{-6}	-
21	Initial heat production	Q_0	$11.67 * [^{26}\text{Al}/^{27}\text{Al}]_0$	W m^{-3}
22	Half-life of ^{26}Al	$t_{1/2}$	0.72	Ma
23	Decay energy per atom	E_{Al}	5.1×10^{-13}	J
24	Aluminum mass fraction	m_{Al}	0.0101	-

25

26 Thereby, the initial heat production per 1 m^3 follows from the aluminium mass fraction of
27 0.0101 (see the reference Loveland 1969 in Miyamoto et al. 1981).

28

29
30
31
32



33 **Fig. S.1:** Temperature evolution at different depths. The lines correspond to the distances
34 from centre of 0 (solid), 55 (dashed), 77 (dotted) and 82.5 (dot-dashed) km. The lines coincide
35 with those of Figure 1 (a) from Miyamoto et al. (1981).

36 **2 Šrámek et al. 2012 (conduction only)**

37 Parameters

38	Radius	R	500	km
39	Formation time rel. to CAIs	t_0	0, 1, 2	Ma
40	Fe volume fraction	v_{Fe}	0.18	-
41	Si volume fraction	v_{Si}	0.82	-
42	Fe thermal conductivity	k_{Fe}	50	$W m^{-1} K^{-1}$
43	Si thermal conductivity	k_{Si}	3	$W m^{-1} K^{-1}$
44	Fe density	ρ_{Fe}	7800	$kg m^{-3}$
45	Si density	ρ_{Si}	3200	$kg m^{-3}$
46	Fe specific heat capacity	$c_{p,Fe}$	450	$J kg^{-1} K^{-1}$
47	Si specific heat capacity	$c_{p,Si}$	1200	$J kg^{-1} K^{-1}$
48	Initial / surface temperature	T_0, T_N	300	K
49	Porosity	ϕ	0	-
50	Initial ratio $^{26}Al/^{27}Al$	$[^{26}Al/^{27}Al]_0$	5.0×10^{-5}	-
51	Initial heat production	Q_0	1.5×10^{-7}	$W kg^{-1}$
52	Half-life of ^{26}Al	$t_{1/2}$	0.717	Ma
53	Decay energy per atom	E_{Al}	5.1×10^{-13}	J
54	Aluminum mass fraction	m_{Al}	0.00865	-

55

56 Thereby, the average values of the mixture are calculated as volume fraction weighted
57 averages of the respective values of Fe and Si.

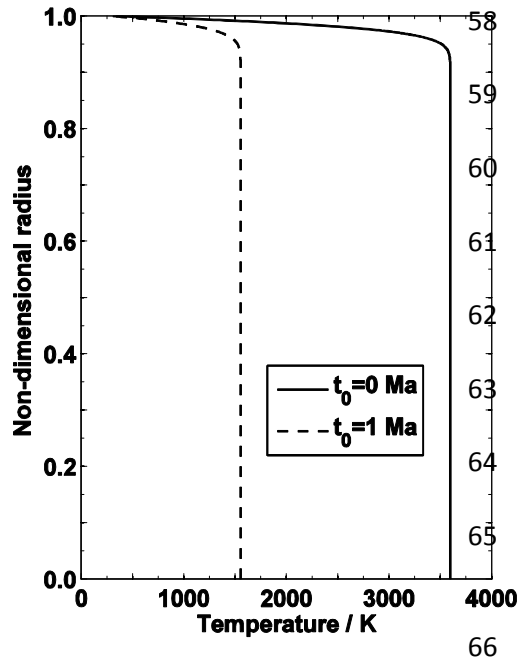


Fig. S.2: Results of the computations performed using our code with the parameters from above. The lines show temperature as function of normalised radius at 1 Ma after the formation. The formation times are $t_0 = 0$ Ma (solid line) and $t_0 = 1$ Ma (dashed line) relative to the formation of the CAIs. The temperature profiles are identical to those in Fig. 1 in Šrámek et al. 2012 (thin solid and thin dashed lines).

67 **3 Moskovitz and Gaidos (2011) (melting, latent heat consumption and release, no**
68 **differentiation)**

69 Parameters

70	Radius	R	50	km
71	Formation time rel. to CAIs	t_0	1	Ma
72	Thermal conductivity	k	2.1	$\text{W m}^{-1} \text{K}^{-1}$
73	Density	ρ	3300	kg m^{-3}
74	Matrix specific heat capacity	$c_{p,s}$	800	$\text{J kg}^{-1} \text{K}^{-1}$
75	Melt specific heat capacity	$c_{p,m}$	2000	$\text{J kg}^{-1} \text{K}^{-1}$
76	Initial / surface temperature	T_0, T_N	180	K
77	Porosity	ϕ	0	-
78	Initial abundance of ^{26}Al	f_{Al}	2.62×10^{23}	kg^{-1}
79	Initial ratio $^{26}\text{Al}/^{27}\text{Al}$	$[^{26}\text{Al}/^{27}\text{Al}]_0$	5.0×10^{-5}	-
80	Decay energy per atom	E_{Al}	6.4154×10^{-13}	J
81	Half-life of ^{26}Al	$t_{1/2}$	0.74	Ma
82	Initial abundance of ^{60}Fe	f_{Fe}	2.41×10^{24}	kg^{-1}
83	Initial ratio $^{60}\text{Fe}/^{56}\text{Fe}$	$[^{60}\text{Fe}/^{56}\text{Fe}]_0$	6.0×10^{-7}	-
84	Decay energy per atom	E_{Al}	4.87×10^{-13}	J
85	Half-life of ^{60}Fe	$t_{1/2}$	2.62	Ma
86	Solidus temperature	T_S	1373	K
87	Liquidus temperature	T_L	2009	K
88	Latent heat of Si	L	400	kJ kg^{-1}

89 Above T_L the effective specific heat capacity is computed as melt fraction weighted average
90 of the heat capacities of the matrix and the melt. Thereby, the melt fraction χ is calculated

91 from an empirical fit to the fertility function of peridotite (see reference McKenzie and Bickle
92 1988 in Moskovitz and Gaidos 2011):

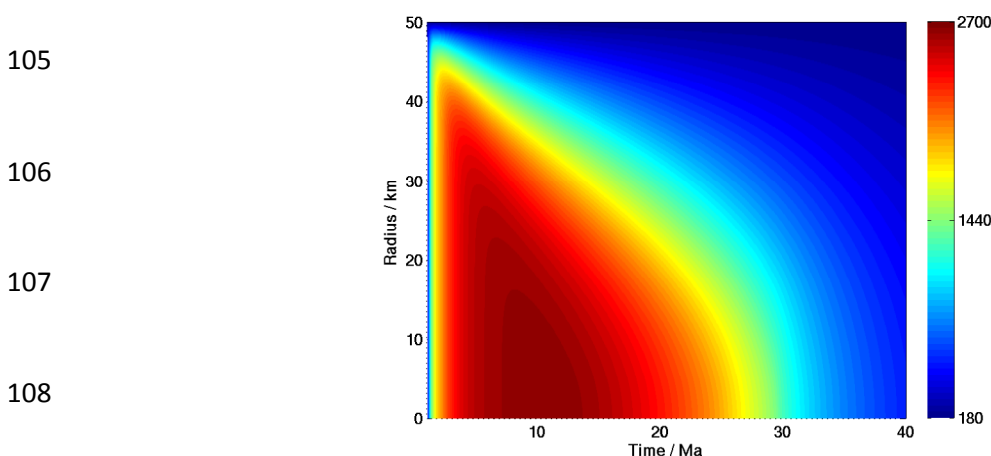
$$93 \chi(T',T) = 0.3936 + 0.253 * T' + 0.4256 * T'^2 + 2.988 * T'^3,$$

94 where

$$95 T'(T) = (T - 1691) / 636.$$

96 Here, $636 = T_L - T_S$, and $1691 = (T_S + T_L) / 2$. Note that although $(T_S + T_L) / 2 = 1418.1$ is stated in
97 Moskovitz and Gaidos (2011), the correct value of 1691 follows from McKenzie and Bickle
98 (1988) and, as far as our calculations show, the correct value seems to have been adopted in
99 Moskovitz and Gaidos (2011).

100 We have used this fit $\chi(T')$ to produce melt in our model. The derivative $d\chi(T')/dT$ represents
101 the melting rate. This was used to derive the Stefan number (instead of using the melting rate
102 $1/(T_L - T_S)$ which follows from the linear melting which is assumed in our model). No latent
103 heat consumption or release due to metal melting or solidification was assumed, as the model
104 by Moskovitz and Gaidos (2011) considers a homogeneous body.



105
106
107
108
109 **Fig. S.3:** Temperature evolution for an $R = 50$ km planetesimal that accreted 1.0 Ma after
110 CAI formation. According to Moskovitz and Gaidos (2011) their Fig. 1, the onset of melting
111 occurs at 1.3 Ma after the formation of CAIs, at 11 Ma a peak temperature of 2615 K is

112 reached, and by 29 Ma the entire body cools to below the silicate solidus. In the simulation
 113 performed with our code, onset of melting occurs at 1.34 Ma, the maximum temperature of
 114 2656 K is reached at 10.65 Ma, and by 29.5 Ma the entire body cools to below the silicate
 115 solidus. The difference between the maximum temperatures between Moskovitz and Gaidos
 116 (2011) and our simulation is approximately 1.5 %.

117 **4. Merk et al. (2002) (melting, latent heat consumption and release, no differentiation)**

118 Parameters:

119	Radius	R	5 - 105	km
120	Formation time rel. to CAIs	t_0	0 - 1.44	Ma
121	Thermal conductivity	k	3.31	$\text{W m}^{-1} \text{K}^{-1}$
122	Density	ρ	3810	kg m^{-3}
123	Matrix specific heat capacity	$c_{p,s}$	Debye	$\text{J kg}^{-1} \text{K}^{-1}$
124	Melt specific heat capacity	$c_{p,m}$	2000	$\text{J kg}^{-1} \text{K}^{-1}$
125	Initial / surface temperature	T_0, T_N	290	K
126	Porosity	ϕ	0	-
127	Initial ratio $^{26}\text{Al}/^{27}\text{Al}$	$[\text{}^{26}\text{Al}/\text{}^{27}\text{Al}]_0$	5.0×10^{-5}	-
128	Initial heat production	Q_0	$13.89 * [\text{}^{26}\text{Al}/\text{}^{27}\text{Al}]_0$	W m^{-3}
129	Half-life of ^{26}Al	$t_{1/2}$	0.72	Ma
130	Solidus temperature	T_S	1425	K
131	Liquidus temperature	T_L	1850	K
132	Latent heat of Si	L	400	kJ kg^{-1}

133 The treatment of consumption and release of latent heat in our model is identical to that in
 134 Merk et al. (2002). However, in Merk et al. (2002) the specific heat capacity of the solid
 135 matrix is obtained from the Debye law. We implemented the Debye law to be as close to this
 136 model as possible. Unfortunately, the value of the Debye temperature used is not stated in
 137 Merk et al. (2002). For temperatures above the solidus temperature T_S , the melt fraction
 138 weighted average of the respective specific heats $c_{p,s}$ and $c_{p,m}$ is used. Merk et al. (2002)
 139 adopted the procedure described by Miyamoto et al. (1981) for calculating Q_0 . Here one needs
 140 to account for a different density of the body, thus the value 11.67 from Miyamoto et al.
 141 (1981) is scaled with the density ratio of 3810/3200 to obtain the value 13.89 from the upper
 142 table.

143
144
145
146
147
148
149
150
151
152
153
154
155
156
157
158
159
160
161
162
163
164
165
166
167
168
169
170

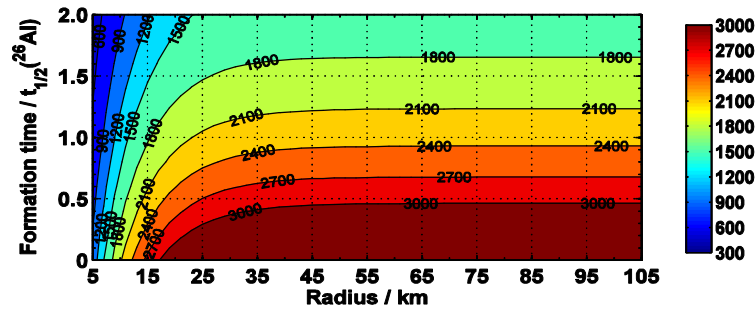


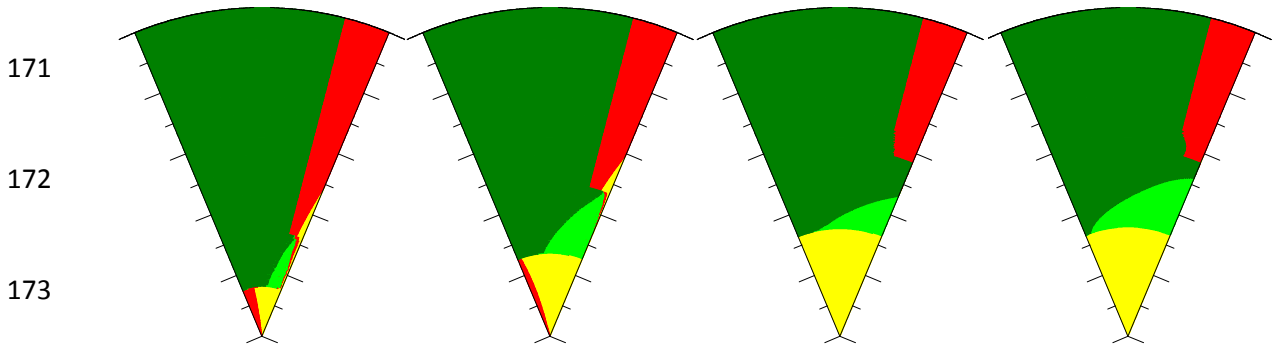
Fig. S.4: Maximum central temperature in planetesimals with the radii 5 – 105 km which accrete instantaneously at formation times $t_0 \leq 2 \cdot t_{1/2} (^{26}\text{Al})$. There are minor shifts of the contour lines by less than 0.1 Ma on this plot compared to Fig. 1 in Merk et al. (2002), probably due to the unknown chosen value of the Debye temperature. Also, the lines in Merk et al. (2002) are broken due to the coarse resolution along the x-axis.

5 Šrámek et al. (2012) (accretion and differentiation)

Additional parameters apart from those given in section A.1.2.

Initial radius	R_0	5	km
Final radius	R	500	km
Accretion onset time rel. to CAIs	t_0	0	Ma
Accretion duration	t_a	3	Ma
Accretion law	-	linear	-
Fe melting temperature	T_{Fe}	1261	K
Si melting temperature	T_{Si}	1408	K
Fe melt viscosity	η_{Fe}	1	Pa s
Latent heat of Fe	L_{Fe}	250	kJ kg^{-1}
Latent heat of Si	L_{Si}	500	kJ kg^{-1}

It should be noted that the approach on the melting process and on the consumption and release of latent heat in Šrámek et al. (2012) is completely different from ours. Also the differentiation process is modeled in another way within the framework of a two-phase flow model (although the basic idea of the density contrast as the driving force of melt percolation is the same). The goal of this comparison is to clarify, whether, in spite of all the differences, the intermediate and final structures produced by the differentiation process correspond to each other approximately, even in a rather complex case where a body accretes and differentiates simultaneously.



174 **Fig. S.5:** Volume fractions of solid metal (red), liquid metal (yellow), solid silicate (dark
 175 green), liquid silicate (light green) of the body described above at different times during and
 176 after its accretion (from left to right the times are: $t = 0.4, 0.6, 3.0$ and 20.0 Ma). Although the
 177 actual radius of the body increases, normalised radius is used for clarity. In our simulation a
 178 slightly smaller core and a thicker undifferentiated layer was obtained compared to Šrámek et
 179 al. (2012), Fig. 7.

180 Numerical issues

181 1 Time discretisation

182 We utilise the minimum of two different time steps (associated to heat conduction and melt

183 percolation) $\Delta t \leq \min(\Delta t_c, \Delta t_m)$. Here, $\Delta t_c \leq 0.5 \frac{\rho c_p}{k} (1 + x_{Fe} Ste_{Fe} + x_{Si} Ste_{Si}) (\Delta x)^2$, where k is

184 either the local thermal conductivity, or the effective thermal conductivity (if convection takes

185 place) and $\Delta t_m \leq \min\left(\frac{\Delta x}{\Delta v_{Fe}}, \frac{\Delta x}{\Delta v_{Si}}\right)$. Both time steps are computed locally for each grid point

186 of the radial discretisation, due to the variations in the spatial resolution and in the material

187 properties. Subsequently the minimum over all grid points is adopted as the actual time step.

188 Also, if during the convection in the core the heat flux at the CMB falls below the adiabatic

189 one, the time step is not increased to the full value Δt_c for the non-effective conductivity, but

190 kept at the last value where k_{eff} was involved, until convection proceeds.

191 2 Spatial resolution

192 The spatial resolution in the models presented in the study was set to 490 m in the interior and
193 160 m in the outer 25 radius% of the body (for the compacted reference). The fine resolution
194 of the shallow regions is due to the extra-thin structures and sharp gradients in the temperature
195 and porosity. If the resolution of the crustal region is too rough, the cooling and crystallisation
196 of the melt in the shallow regions on its way to the surface is underestimated. Thus, eruptions
197 occur where there should be none, and a basaltic crust forms, although the surface should
198 remain primordial. On the other hand, if the resolution is too fine (e.g. 10 m), then no
199 eruptions and basaltic crust formation will occur at all by porous flow, because of the
200 effective cooling at the depth of 10 m. This is in principal possible; however, melt migration
201 to the surface via dykes and cracks through such a thin layer is most likely. Because dykes
202 have not been implemented in our model, the specific choice of resolution of 160 m in the
203 outer 25 radius% is provides a compromise which allows the consideration of both the
204 cooling and crystallisation of the ascending melt and to some extent of the melt migration via
205 dykes. According to our test runs, a more coarse resolution increases the melt percolation rate
206 to the surface and decreases the life-time of the shallow magma ocean, and vice versa.